Mutation of highly conserved residues in loop 2 of the coronavirus macrodomain demonstrates that enhanced ADP-ribose binding is detrimental to infection

Catherine M. Kerr[1*], Jessica J. Pfannenstiel[1*], Yousef M. Alhammad[1], Anuradha Roy[2], Joseph J. O'Connor[1], Roshan Ghimire[3], Reem Khattabi[1], Rakshya Shrestha[3], Peter R. McDonald[2], Philip Gao[4], David K. Johnson[5], Sunil More[3, 6], Rudragouda Channappanavar[3, 6], Anthony R. Fehr[1#]

[1]Department of Molecular Biosciences, University of Kansas, Lawrence, Kansas 66045, USA
[2]High Throughput Screening Laboratory, University of Kansas, Lawrence, Kansas 66047, USA
[3]Department of Veterinary Pathobiology, Oklahoma State University, Stillwater, Oklahoma 74078, USA
[4]Protein Production Group, University of Kansas, Lawrence, Kansas 66047, USA
[5]Molecular Graphics and Modeling Laboratory and the Computational Chemical Biology Core, University of Kansas, Lawrence, Kansas 66047, USA
[6]Oklahoma Center for Respiratory and Infectious Diseases, College of Veterinary Medicine, Stillwater, Oklahoma 74078, USA

[*]These authors contributed equally to this work. Author order was determined by relative contributions to writing the manuscript.

[#]Correspondence: arfehr@ku.edu; Tel.: +1-(785) 864-6626 (K.S.)

Running title: Increased Mac1 ADP-ribose binding attenuates CoV infection

Keywords: coronavirus, MERS-CoV, SARS-CoV-2, MHV, non-structural protein 3, macrodomain, ADP-ribosylation, ADP-ribosylhydrolase, interferon

ABSTRACT

All coronaviruses (CoVs) encode for a conserved macrodomain (Mac1) located in nonstructural protein 3 (nsp3). Mac1 is an ADP-ribosylhydrolase that binds and hydrolyzes mono-ADP-ribose from target proteins. Previous work has shown that Mac1 is important for virus replication and pathogenesis. Within Mac1, there are several regions that are highly conserved across CoVs, including the GIF (glycine-isoleucine-phenylalanine) motif. To determine how the biochemical activities of these residues impact CoV replication, the isoleucine and the phenylalanine residues were mutated to alanine (I-A/F-A) in both recombinant Mac1 proteins and recombinant CoVs, including murine hepatitis virus (MHV), Middle East respiratory syndrome coronavirus (MERS-CoV), and severe acute respiratory syndrome coronavirus 2 (SARS-CoV-2). The F-A mutant proteins had ADP-ribose binding and/or hydrolysis defects that led to attenuated replication and pathogenesis in cell culture and mice. In contrast, the I-A mutations had normal enzyme activity and enhanced ADP-ribose binding. Despite increased ADP-ribose binding, I-A mutant MERS-CoV and SARS-CoV-2 were highly attenuated in both cell culture and mice, indicating that this isoleucine residue acts as a gate that controls ADP-ribose binding for efficient virus replication. These results highlight the function of this highly conserved residue and provide unique insight into how macrodomains control ADP-ribose binding and hydrolysis to promote viral replication and pathogenesis.

46 **INTRODUCTION**

47 Coronaviruses (CoVs), from the family *Coronaviridae* of the order *Nidovirales*, are large
48 positive-sense RNA viruses of both human and veterinary significance. In the past few decades,
49 there have been three significant outbreaks of lethal human CoV disease. The first outbreak
50 occurred in 2002-2003 when severe acute respiratory syndrome (SARS-CoV) emerged in China.
51 In 2012, Middle East respiratory syndrome (MERS)-CoV was reported in Saudi Arabia. More
52 recently, in late 2019, the SARS-CoV-2 emerged in Wuhan, China and rapidly spread around the
53 world, becoming the first CoV to be the cause of a pandemic [1].

54 CoVs genomes range in size from 26-32 kb and encode for four conserved structural
55 proteins, up to ten accessory proteins, and 15-16 non-structural proteins (nsps) that are expressed
56 in two polyproteins, polyprotein 1 a (pp1a) and polyprotein 1 ab (pp1ab). These polyproteins are
57 further cleaved by viral proteases into individual non-structural proteins. The nsps encode for a
58 variety of proteins that are necessary for replication and innate immune evasion, such as the RNA-
59 dependent RNA polymerase, main protease, helicase, N-7 methyltransferase, exoribonuclease, an
60 endoribonuclease, and many others. The largest of the CoV nsps is nsp3, which forms a pore within
61 the replication transcription complexes (RTCs) [2] and encodes for multiple modular domains,
62 including ubiquitin-like domains, one or two papain-like protease domains, a deubiquitinase
63 domain, a CoV-Y domain, and one or more macrodomains [3, 4].

64 Some CoVs encode for as many as 3 tandem macrodomains, termed Mac1, Mac2, and
65 Mac3. Mac1 is a conserved domain found in all CoVs, Togaviruses, Rubiviruses, and Hepatitis E
66 virus [5]. The highly conserved structure of Mac1 consists of several central β-sheets surrounded
67 by 3 α-helices on each side [6-10]. Mac1 has been shown to reverse host ADP-ribosylation of
68 target proteins [11, 12]. ADP-ribosylation is a common posttranslational modification that is

69 catalyzed by ADP-ribosyltransferases (ARTs) that utilize NAD^+ to covalently attach a single ADP-
70 ribose unit, mono-ADP-ribosylation (MARylaytion/MAR), or a chain of several ADP-ribose units,
71 poly-ADP-ribosylation (PARylation/PAR) to a target protein or nucleic acid [13, 14]. These
72 modifications are crucial for cellular stress responses, including viral infections [15]. The most
73 common mammalian ARTs are PARPs, and the most well studied PARP is PARP1, which is a
74 target of anti-cancer drugs due to its role in the DNA damage response. However, most PARPs are
75 MARylating PARPs, many of which are IFN-stimulated genes (ISGs) and are known to impact
76 virus infections [16].

77 Several studies have demonstrated that the conserved macrodomain is critical for CoV,
78 alphavirus, and Hepatitis E virus infection, using either deletion or point mutations of the
79 conserved macrodomain [11, 17-25], indicating that these viruses are especially sensitive to host
80 PARP-mediated antiviral functions. However, despite clear evidence that Mac1 is critical for CoV
81 infection, there have only been a few studies that have investigated how individual residues
82 contribute to the biochemical functions of Mac1 and how those biochemical activities correlate
83 with CoV replication and pathogenesis. Initial studies of Mac1 in CoVs focused on the mutation
84 of a highly conserved asparagine residue to alanine or aspartic acid. This mutation largely impairs
85 Mac1 deMARylating activity, as has been demonstrated for the α-CoV 229E, and the β-CoVs
86 SARS-CoV, and SARS-CoV-2 proteins [8, 11, 24, 26]. In most cases, these mutations did not
87 significantly reduce virus replication in cell culture but did lead to highly attenuated viruses in
88 mice [11, 20, 21, 24, 26]. We also showed that the Asn-to-Ala mutation in the β-CoV murine
89 hepatitis virus strain JHM (MHV) led to poor replication in primary bone-marrow-derived
90 macrophages, which was reversed upon either knockdown or knockout of PARP12, demonstrating
91 that Mac1 specifically counters PARP activity [27, 28]. Furthermore, overexpression of SARS-

92 CoV-2 WT Mac1, but not the asparagine-to-alanine mutation, reverses PARP9/DTX3L mediated
93 ADP-ribosylation following IFN or poly(I:C) treatment [29]. In addition, the same mutation in
94 SARS-CoV-2 (N1062A) was more sensitive to IFNγ treatment in cell culture and was attenuated
95 *in vivo* [19]. The only other mutations that have been evaluated both in the context of biochemical
96 activity and virus replication are D1022A, H1045A, and G1130V (all numbers based on the SARS-
97 CoV Mac1) [11, 26]. In the context of SARS-CoV, each of these mutations had reduced ADP-
98 ribosylhydrolase activity, replicated normally in cell culture, and were attenuated in mice [11]. A
99 later study evaluated the role of the D1329A and G1439V mutations in MHV. Recombinant viruses
100 with those mutations, which are predicted to dramatically reduce Mac1 ADP-ribose binding, were
101 highly attenuated in cell culture, much more so than the aforementioned N1347A mutation [30].
102 These results indicated that ADP-ribose binding may be more critical for MHV than for SARS-
103 CoV. This was further confirmed with SARS-CoV-2, as the orthologous D1044A mutation did not
104 display increased sensitivity to IFNγ and was only partially attenuated in mice [19].

105 The highly conserved isoleucine and phenylalanine residues in loop 2 are also of great
106 interest due to their conservation and positioning within the ADP-ribose binding pocket (Fig. 1A-
107 B) [6, 8, 10], though the impact of these residues on CoV replication has not been addressed. The
108 isoleucine appears to interact with the final glycine in loop 1 to form a narrow channel around the
109 diphosphate within the ADP-ribose binding domain that could be important for both binding and
110 hydrolysis. In contrast, the phenylalanine residue makes van der Waals interactions with the distal
111 ribose and orients the distal ribose for hydrolysis. In prior studies, mutation of phenylalanine-to-
112 leucine reduced enzyme activity of SARS-CoV-2 Mac1 as expected, while an isoleucine-to-alanine
113 mutation of the SARS-CoV-2 or HKU4 Mac1 did not impact enzyme activity [8, 31]. It remains

114 unclear how these residues impact ADP-ribose binding and ultimately how their biochemical
115 functions relate to virus replication and pathogenesis.

116 In this study, we tested how mutations of the isoleucine (I) and phenylalanine (F) residues
117 in loop 2 of the CoV Mac1 (Fig. 1A-B) impact both Mac1 biochemical functions and the
118 replication and pathogenesis of *Embeco*, *Merbeco*, and *Sarbeco* lineages of β-CoVs. While F-A
119 mutations resulted in poor enzyme activity and attenuated viruses, I-A mutations surprisingly led
120 to enhanced ADP-ribose binding with little-to-no effect on its enzyme activity. More remarkably,
121 this enhanced binding was detrimental to its biological function, as recombinant MERS-CoV and
122 SARS-CoV-2 viruses with the I-A mutation were highly attenuated. We hypothesize that this
123 isoleucine residue acts as a gate to control ADP-ribose binding and maintain proper enzyme
124 activity during infection. These results provide a rare example where enhancing the biochemical
125 function of a protein has a negative impact on its biological function.

126 **RESULTS**

127 **Murine hepatitis strain JHM (MHV) F1441A, but not I1440A, has decreased replication in**
128 **cell culture and in mice.** To uncover the relative contributions of the residues in the highly
129 conserved GIF loop of Mac1 in CoV replication and pathogenesis, we first compared the
130 replication of the *Embecovirus* MHV I1440A and F1441A mutations to WT and a previously
131 characterized mutant virus, N1347A. Previously, we found that N1347A replicates normally in
132 most cell lines susceptible to MHV but replicates poorly in primary macrophages and in mice [21,
133 27]. Here, we tested the replication of recombinant viruses in several different cell types that are
134 susceptible to MHV including: a mouse astrocyte cell line (DBT), a mouse fibroblast cell line
135 (L929), and primary bone-marrow cells differentiated into M2 macrophages. As expected, the
136 F1441A mutation had decreased replication in all cell types and in mice, with replication defects

137 seen at peak titers ranging from 2.7-fold in DBT cells, to 4.3-fold in L929 cells, and 21.7-fold in
138 M2 macrophages (Fig. 2A-C). We previously found that a knockout (KO) of PARP12 can restore
139 the replication of N1347A, therefore we also tested the ability of F1441A to replicate in PARP12
140 KO M2 BMDMs (Fig. 2D). In the absence of PARP12, F1441A replication increased by 9.3-fold,
141 indicating that PARP12 contributes to the restriction of this virus, much like N1347A. However,
142 it was not fully rescued, indicating that F1441 may also be important for ADP-ribose binding. In
143 contrast, I1440A replicated at WT levels in all cell types and at all time points (Fig. 2A-D).

144 We hypothesized that the importance of the isoleucine residue may become more apparent
145 *in vivo*, so we tested the ability of these mutant MHV to cause severe encephalitis in mice.
146 C57BL/6 mice were infected intranasally with 10^4 PFU of each virus and were monitored for
147 weight loss and survival over 12 days, and viral loads in the brain were measured at day 5 post-
148 infection. The F1441A mutant was attenuated in mice as only 50% of the mice succumbed to
149 infection, while the other half recovered after losing ~10% of their body weight (Fig. 3A and B).
150 This attenuation of F1441A was also demonstrated in the disease scores of the F1441A virus, as
151 disease scores started to reverse by day 8 for F1441A infected mice (Fig. 3C). Furthermore,
152 F1441A virus infected mice had ~7.5 fold lower viral loads in mice than WT virus infected mice
153 (Fig. 3D). These titers were highly variable, reflecting the fact that 50% of the mice survived. In
154 contrast, I1440A infected mice all succumbed to disease by 9 dpi, and much like the cell culture
155 results, the I1440A viral loads were equivalent to WT virus in mice (Fig. 3A-D). Taken together,
156 this indicates that F1441 is required for efficient virus replication and disease progression in
157 JHMV, while the I1440 residue does not impact JHMV replication or pathogenesis. The lack of
158 any impact of the I1440A mutation on MHV replication or pathogenesis was surprising,
159 considering the extreme conservation of this residue through all CoVs [5].

160 **MERS-CoV I238A has increased binding activity.** To determine how these mutations impact
161 the biochemical functions of Mac1, we aimed to purify Mac1 protein with these mutations and
162 utilize *in vitro* assays to measure ADP-ribosylhydrolase and ADP-ribose binding activity of each
163 mutant protein. Multiple attempts to produce MHV Mac1 protein failed, so we engineered these
164 mutations into the *Merbecovirus* MERS-CoV and the *Sarbecovirus* SARS-CoV-2 Mac1
165 recombinant proteins, as we've previously produced WT Mac1 proteins from each virus [6]. We
166 first produced soluble I1238A and F1239A MERS-CoV Mac1 proteins and performed isothermal
167 titration calorimetry (ITC) to measure Mac1-ADP-ribose binding. ITC measures the release or
168 absorption of energy during a binding reaction and has been used extensively to measure
169 macrodomain-ADP-ribose interactions [6, 18, 22, 32, 33]. Compared to WT protein, the F1239A
170 protein bound to free ADP-ribose with a substantially higher K_D value (60 μM vs. 7.2 μM)
171 indicating reduced binding ability. In contrast, the I1238A protein bound to ADP-ribose with a K_D
172 nearly equivalent to that of WT (12.7 μM vs 7.2 μM) (Fig. 4A). In addition to ITC, we also
173 performed an AlphaScreen assay, as previously described [34-36], to determine the ability of each
174 protein to bind to an ADP-ribosylated peptide. Similar to the ITC assay, the F1239A Mac1 had
175 substantially reduced AlphaScreen counts at all concentrations of protein tested as compared to
176 WT protein, indicating poor binding to the ADP-ribosylated peptide (Fig. 4B). Remarkably, the
177 I1238A Mac1 protein had dramatically increased AlphaScreen counts at all concentrations of
178 protein tested, indicating that this mutation has enhanced binding to an ADP-ribosylated peptide
179 (Fig. 4B). To further test this observation, we performed a competition assay by adding increasing
180 amounts of ADP-ribose to the reaction. ADP-ribose inhibited the peptide-ADP-ribose interaction
181 of WT MERS-CoV protein with an average IC_{50} value, of 0.155 μM, while it had a much higher

182 IC_{50} value of 1.6 μM for the I1238A protein. These results demonstrate that I1238A had a stronger
183 interaction with the ADP-ribosylated peptide than WT protein (Fig. 4C).

184 We next tested the ability of the MERS-CoV I1238A and F1238A Mac1 proteins to
185 hydrolyze mono-ADP-ribose (MAR) from protein as previously described [6]. The WT, I1238A,
186 and F1239A Mac1 proteins were incubated with MARylated PARP10 at a 1:5 enzyme to substrate
187 ([E]/[S]) ratio, and the reaction was stopped at several timepoints to determine the ability of each
188 protein to hydrolyze MAR. As a control, MARylated PARP10 was collected at the first (0 min)
189 and the final (30 min) timepoints. Over the course of 30 minutes, the MERS-CoV I1238A Mac1
190 protein decreased the level of MARylated PARP10 to similar levels of the MERS-CoV WT Mac1
191 protein, while the MERS-CoV F1239A Mac1 protein did not efficiently remove the MARylation
192 from PARP10 (Fig. 4D-E). Taken together, we conclude that the MERS-CoV I1238A and F1239A
193 mutations had somewhat opposing effects on the activity of Mac1. While F1239A mutant Mac1
194 protein has decreased ADP-ribose binding and hydrolysis activity, the I1238A Mac1 has increased
195 ADP-ribose binding with only a modest reduction in enzyme activity compared to the MERS-CoV
196 WT Mac1 (Table 1).

197 **MERS-CoV I1238A and F1239A viruses have decreased replication in human and bat cell**
198 **lines.** With biochemical results in hand, we next tested MERS-CoV I1238A and F1239A viruses
199 for their ability to replicate in multiple cell types. First, using recombination, we inserted a GFP
200 cassette in place of ORF5 in the MERS-CoV-MA BAC, as ORF5 quickly mutates in cell culture,
201 which could complicate our results [37, 38]. Considering that the I1238A had equivalent or
202 enhanced biochemical activities compared to WT protein, we hypothesized that only the F1239A
203 virus would impact MERS-CoV replication, similar to results seen with MHV (Figs 2-3). Both
204 mutant viruses replicated near WT levels at all time points in Vero81 cells, which are unable to

205 produce interferon (IFN) (Fig. 5A). Next, we tested the replication of these viruses in IFN-
206 competent Calu3 cells, human bronchial epithelial cells, and AJK6 cells, a Jamaican bat kidney
207 cell line previously shown to be susceptible to MERS-CoV. To our surprise, both viruses replicated
208 poorly in these cells. In Calu3 cells F1239A replicated at 4.7 and 46.7-fold lower than WT virus
209 at 48 and 72 hours, respectively, while I1238A replication was reduced 5.3 and 34.1-fold at 48 and
210 72 hpi (Fig. 5B). In the AJK6 cells, the F1239A virus had replication defects of 2.5 and 12-fold at
211 24 and 48 hours respectively, while the I1238A virus replicated was reduced 18.5-fold at 48 hpi
212 (Fig. 5C). We conclude that each of these residues is critical for MERS-CoV replication in cell
213 culture, and that the defect of the I1238A virus could be due to enhanced ADP-ribose binding
214 (Table 1).

215 **SARS-CoV-2 I1153A and F1154A have increased ADP-ribose binding activity.** The MERS-
216 CoV data indicated that increased ADP-ribose binding activity may lead to replication defects in
217 culture. However, each of the MERS-CoV mutants had at least a modest defect in enzyme activity,
218 which could account for the poor replication of each virus (Table 1). To further test the hypothesis
219 that increased ADP-ribose binding could be detrimental to infection, we engineered these
220 mutations in SARS-CoV-2 to analyze their impact on Mac1 biochemical functions and viral
221 replication. We produced soluble I1153A and the F1154A SARS-CoV-2 Mac1 proteins and first
222 performed ITC to determine the ADP-ribose binding ability of each Mac1 mutant protein.
223 Interestingly, both the SARS-CoV-2 I1153A and the F1154A Mac1 proteins had increased binding
224 to free ADP-ribose, with K_D values of 5.49 μM and 5.11 μM, respectively, compared to the K_D
225 value of 16.8 μM for WT protein (Fig. 6A). Next, we tested the ability of each protein to bind to
226 the ADP-ribosylated peptide in the AlphaScreen assay. Again, we observed that both the I1153A

227 and the F1154A Mac1 proteins had increased binding to the ADP-ribosylated peptide compared
228 to the WT Mac1 protein (Fig. 6B).

229 Next, we tested the ability of each SARS-CoV-2 protein to remove MAR from MARylated
230 PARP10, again at a 1:5 [E]/[S] ratio to account for defects in enzyme turnover. Like MERS-CoV
231 F1239A, SARS-CoV-2 F1154A had only modest hydrolysis activity. In contrast, I1153A Mac1
232 protein had robust enzymatic activity, which was virtually indistinguishable from WT protein (Fig.
233 6C-D), which is consistent with previously published results [8]. These results demonstrate that
234 the I1153A and F1154A both have enhanced ADP-ribose binding, but that only F1154A has
235 reduced enzymatic activity (Table 1).

236 As many previous studies of Mac1 in virus replication include the highly conserved
237 asparagine-to-alanine mutation, we also generated an N1062A SARS-CoV-2 Mac1 protein. This
238 protein is highly unstable, so several modifications to the normal protocol were made to create a
239 small amount of soluble protein. While the small amount of protein did not allow for ITC
240 measurements, this protein had similar ADP-ribose binding properties as WT protein, as
241 determined by the alphascreen, ADP-ribose competition, and differential scanning fluorimetry
242 assays (Fig. 7A-C). In contrast, this protein had substantially reduced ADP-ribosylhydrolase
243 activity (Fig. 7D-E), indicating that this mutation primarily impacts the enzyme activity of Mac1.
244 Previously published biochemical data also supports the hypothesis that this mutation primarily
245 impacts the enzyme activity of Mac1 [10, 11, 18, 24, 26, 32]. This mutation can be directly
246 compared with F1154A to determine the impact of increased ADP-ribose binding on virus
247 replication and pathogenesis, as both F1154A and N1062A have similar defects in enzyme activity
248 but only F1154A has increased ADP-ribose binding (Table 1).

249 **Increased Mac1 ADP-ribose binding increases the sensitivity of SARS-CoV-2 to IFNγ.** We
250 previously reported that a Mac1 deleted SARS-CoV-2 is highly sensitive to IFNγ pretreatment in
251 Calu-3 cells. After demonstrating that both the SARS-CoV-2 I1153A and F1154A Mac1 proteins
252 have increased ADP-ribose binding, we next tested the ability of these recombinant viruses to
253 replicate in the presence of IFNγ. Without IFNγ pre-treatment at 48 hpi, both I1153A and F1154A
254 replicate at WT levels (Fig. 8A). In contrast, there is a substantial decrease in both I1153A and
255 F1154A replication in both cell lines compared to WT SARS-CoV-2 in the presence of IFNγ (Fig.
256 8A-B). Furthermore, mutation at the N1062 residue, which primarily reduces ADP-
257 ribosylhydrolase activity, has increased sensitivity to IFNγ as well, though not as severe as the
258 I1153A and F1154A mutant viruses [19]. These results support a model where Mac1 enzyme
259 activity is primarily responsible for its ability to counter IFNγ-mediated antiviral responses, and
260 based on results with I1153A, that increased ADP-ribose binding may negatively affect Mac1's
261 ability to hydrolyze protein substrates in cells. We conclude that increased ADP-ribose binding by
262 Mac1 is detrimental for the ability of SARS-CoV-2 to replicate efficiently in the presence of IFNγ.
263 **SARS-CoV-2 I1153A and F1154A are attenuated in K18-ACE2 mice.** Next, we tested whether
264 enhanced ADP-ribose binding activity would be detrimental to SARS-CoV-2 infection in mice.
265 Previously, a SARS-CoV-2 Mac1 deletion virus was shown to be extremely attenuated in K18-
266 ACE2 mice, while the N1062A mutant was mildly attenuated, with approximately 50% of mice
267 surviving the infection [19, 24]. We hypothesized that like the SARS-CoV-2 N1062A mutant, there
268 would be at least partial attenuation of I1153A and F1154A viruses in mice. Following an intranasal
269 infection, we were surprised to see that both the SARS-CoV-2 I1153A and F1154A viruses were
270 extremely attenuated in mice, as they did not cause any weight loss or lethal disease in mice,
271 similar to *Δ*Mac1, whereas WT SARS-CoV-2 causes 100% mortality by 9 dpi (Fig. 9A-B). Viral

272 titers were reduced by ~4-5 fold at 1 dpi (Fig. 9C), and by 8 dpi both the I1153A and F1154A
273 viruses were cleared from the lungs of mice (Fig. 9D). Furthermore, mice infected with these
274 viruses had reduced signs of disease, such as bronchointerstitial pneumonia, edema, or fibrin, as
275 measured by H&E staining (Fig. 9E-F). Finally, both I1153A and F1154A infected mice had
276 significantly increased levels of IFN-I, IFN-III, ISG15, and CXCL-10 mRNA, similar to *Δ*Mac1
277 infection levels (Fig. 9G). These results are consistent with the idea that enhanced ADP-ribose
278 binding likely leads to severe defects in deMARylation during infection, as increased cytokine
279 levels were previously demonstrated shown to be due to reduced deMARylating activity of Mac1
280 mutant viruses [24, 30]. Taken together, these results demonstrate that increased ADP-ribose
281 binding by Mac1 is detrimental to SARS-CoV-2 replication and pathogenesis *in vivo*.

282 In total, while the highly conserved isoleucine and phenylalanine mutations in MERS-CoV
283 and SARS-CoV-2 have different effects on Mac1 biochemical activities *in vitro*, their impact on
284 virus replication and pathogenesis were remarkably similar (Table 1). The simplest explanation is
285 that enhanced ADP-ribose binding has a severe effect on Mac1's ability to hydrolyze specific
286 substrates during infection, and that the conserved isoleucine residue acts to control ADP-ribose
287 binding to allow for optimal ADP-ribosylhydrolase activity. But how does this isoleucine residue
288 control ADP-ribose binding? Prior NMR data from the Venezuelan equine encephalitis virus
289 (VEEV) macrodomain indicated that prior to ADP-ribose binding there is a significant transition
290 that increases the distance between loop 1 and loop 2 from 7 to 10 Å to accommodate ADP-ribose
291 as a substrate [39]. We hypothesized that the I1153A protein has increased binding because the
292 protein no longer requires this transition to bind ADP-ribose. To support this hypothesis, we
293 performed a molecular dynamic (MD) simulation of the I1153A and WT proteins in the presence
294 and absence of ADP-ribose and measured the 1 ns running average distance between the I or A

295 1153 residue and G1069 (Fig. 10A-C). In the presence of ADP-ribose, these residues were nearly
296 the same distance apart, ~7.5-8 Å. However, in the absence of ADP-ribose, the mutant protein
297 (A1153) consistently sampled conformations containing a larger distance between these residues,
298 around or longer than ~7.5 Å, which results in a largely open crevice between the two loops (Fig.
299 10A). In contrast, the distance between these residues for the WT protein (I1153) was more often
300 less, even sampling distances below 5 Å (Fig. 10A), and the crevice appears mostly in a closed
301 state, only occasionally opening wide enough to allow for ADP-ribose binding (Fig. 10B-C). These
302 results indicate that the isoleucine residue controls the ability of ADP-ribose to enter the ADP-
303 ribose binding domain.

304 **DISCUSSION**

305 Research on the CoV Mac1 domain over the last two decades has established this protein
306 domain as critical for the replication and pathogenesis of CoVs [40]. However, the relative
307 contributions of its two major biochemical activities, ADP-ribose binding and deMARylation, to
308 its function during infection has remained unclear. Most research on the CoV Mac1 domain has
309 utilized the mutation of a highly-conserved asparagine to alanine. This mutation nearly eliminates
310 the ADP-ribosylhydrolase activity of SARS-CoV Mac1, however, it was previously not clear how
311 much this mutation impacts ADP-ribose binding. Results from archaeal and alphavirus
312 macrodomains have indicated that mutation of the orthologous asparagine residue in those proteins
313 to alanine only modestly reduces ADP-ribose binding [18, 32]. Here we created an N1062A Mac1
314 protein from SARS-CoV-2 and found that it had a severe defect in enzymatic activity, but only had
315 a mild reduction in ADP-ribose binding compared to WT protein (Fig. 7). This confirms that this
316 residue plays a large role in ADP-ribosylhydrolase activity but only minimally impacts ADP-ribose
317 binding. These results further indicate that phenotypes associated with this mutation, including

318 increased IFN production and enhanced sensitivity to IFN-I and IFN-II, are likely due to the loss
319 of ADP-ribosylhydrolase activity.

320 This study focused on the isoleucine and phenylalanine residues located in loop 2 of Mac1,
321 near this asparagine residue. The isoleucine in loop 2 of the CoV Mac1 protein has been described
322 as a bridge that extends from loop 2 to loop 1 that covers the phosphate binding domain of Mac1,
323 forming a narrow channel that might impact binding or hydrolysis [6, 9, 10, 31]. Furthermore, this
324 residue participates in the transition of these loops from the apo form to the ADP-ribose bound
325 form [39], again indicating that this residue may impact ADP-ribose binding. Somewhat
326 surprisingly, we found that an I-A mutation instead led to enhanced ADP-ribose binding based a
327 peptide-ADP-ribose binding assay for both the MERS-CoV and SARS-CoV-2 Mac1 proteins
328 (Figs. 4B-C, 6A-B). Modeling data indicates that with this mutation, the distance between the two
329 loops is consistently large enough that Mac1 can likely accept substrates at any time, as opposed
330 to Mac1 with the isoleucine (Fig. 10A-C). Following ADP-ribose binding, the I-A mutation does
331 not appear to impact the distance between the loops, perhaps explaining why the hydrolysis activity
332 of Mac1 was not affected for either Mac1 protein. These results suggest that the isoleucine residue
333 serves as a gate to control ADP-ribose binding levels.

334 In contrast, the phenylalanine forms van der Waals interactions with the distal ribose, and
335 similar to the nearby asparagine residue, appears to help position the ribose for hydrolysis.
336 Biochemical data has supported those predictions, as mutations of this residue generally result in
337 substantial loss of hydrolysis activity, which we observed here for both the MERS-CoV and SARS-
338 CoV-2 Mac1 proteins (Figs. 4D-E, 6C-D). Interestingly, the F-A mutation had diverse roles in
339 ADP-ribose binding. For MERS-CoV Mac1, this mutation led to reduced binding, while for
340 SARS-CoV-2 this mutation enhanced both free and peptide-conjugated ADP-ribose binding. As

341 the phenylalanine residue resides just outside the terminal ribose, it's conceivable that in some
342 cases this residue may occlude ADP-ribose binding during its transitions, while in others it may
343 be just far enough away to not impact the ability of ADP-ribose to enter the binding pocket [6, 39].
344 While it's unclear how these identical mutations had opposing effects on ADP-ribose binding, it
345 highlights the difficulty in attributing specific biochemical roles for individual residues from one
346 macrodomain to another.

347 Both MERS-CoV and SARS-CoV-2 I-A and F-A mutations were equally attenuated in both
348 cell culture and in mice (Figs. 5, 8, 9) despite having somewhat distinct biochemical properties.
349 The MERS-CoV mutant viruses replicated normally in Vero81 cells but replicated poorly in Calu-
350 3 and AJK6 bat kidney cells, at levels similar to the N1147A virus. This demonstrates that bats
351 also utilize ADP-ribosylation to restrict CoV replication and indicates that loss of enzyme activity
352 during infection may lead to the observed reduction in virus replication. Furthermore, both F-A
353 and I-A SARS-CoV-2 mutant viruses replicated poorly following IFN-γ treatment and induced
354 high levels of IFN and ISG levels following infection in mice, again indicating that increased ADP-
355 ribose binding might lead to poor ADP-ribosylhydrolase activity during infection (Figs. 7, 9). Why
356 might an increase in ADP-ribose binding lead to reduced enzyme activity during infection? One
357 hypothesis would be that enhanced binding would negatively affect enzyme turnover. However,
358 our *in vitro* enzyme assays were performed at an [E]/[S] ratio of 1:5, indicating that the mutant
359 protein has largely normal enzyme turnover. ADP-ribose can be covalently attached to several
360 different amino acids, including cysteine, serine, arginine, glutamic and aspartic acid, but the
361 MacroD2 class of macrodomains primarily removes ADP-ribose from acidic residues. Therefore,
362 a second hypothesis is that enhancing the ADP-ribose binding abilities of Mac1 may cause it to
363 bind to proteins with ADP-ribose attached at non-acidic residues that it can't remove and are not

364 relevant for virus infection. Based on this hypothesis, we propose the following model for both
365 SARS-CoV-2 and MERS-CoV. During infection WT Mac1 primarily engages with either anti- or
366 pro-viral proteins that are MARylated on an acidic residue. Mac1 removes these modifications,
367 which promotes virus replication and pathogenesis. In contrast, Mac1 I-A binds non-specifically
368 to proteins MARylated at non-acidic residues, such as serine or cysteine, reducing its ability to
369 engage with its primary targets. Mac1 becomes stuck to irrelevant targets, while its main target
370 proteins remain ADP-ribosylated, leading to reduced virus replication and increased IFN
371 production (Fig. 10D). Additional experiments will need to be designed to demonstrate that Mac1
372 I-A hydrolysis activity is reduced in a pool of ADP-ribosylated proteins during infection.

373 The function of the isoleucine residue on the MHV Mac1 protein appears to be unique, as
374 the mutation of I-A had little-to-no impact on virus replication. As we have been unable to purify
375 the WT MHV Mac1 protein in bacteria, we can only speculate as to how this mutation impacts
376 ADP-ribose binding and hydrolysis. The simplest hypothesis is that this mutation does not enhance
377 ADP-ribose binding as it did for MERS-CoV or SARS-CoV-2. Alternatively, as MHV appears to
378 be highly dependent on the ADP-ribose binding function of Mac1 [19, 30], an increase in ADP-
379 ribose binding may have some beneficial outcome that counteracts the negative effects of reduced
380 enzyme activity, resulting in a virus that replicates much like WT. Conversely, the F1441A mutant
381 virus replicates poorly in all cells tested and was partially attenuated in mice. It was partially, but
382 not fully, rescued in PARP12 KO cells, which we previously found fully rescued N1347A, but had
383 no effect on D1329A, a mutation predicted to largely impact ADP-ribose binding. Thus, based on
384 these and prior results with N1347A and D1329A, we hypothesize that this mutation reduces both
385 enzyme and binding activity, like the MERS-CoV F1239A Mac1 protein.

386 Typically, an increase in biochemical activity results in an increase in fitness. However,
387 these results highlight a unique case where increasing the biochemical activity of a protein led to
388 a decrease in viral fitness. These results provide new insights into how Mac1 regulates ADP-ribose
389 binding for its benefit, which could have important implications for the development of inhibitors
390 targeting Mac1. Finally, these mutations could be used to help identify the specific targets of Mac1
391 during an infection, which will lead to a better understanding of the mechanisms used by
392 mammalian cells to counter virus infection.

393 **METHODS**

394 **Plasmids.** MERS-CoV Mac1 (residues 1110-1273 of pp1a) and mutations were cloned into
395 pET21a+ with a C-terminal His tag. SARS-CoV-2 Mac1 (residues 1023-1197 of pp1a) was cloned
396 into the pET30a+ expression vector with an N-terminal His tag and a TEV cleavage site (Synbio).
397 **Protein Expression and Purification.** A single colony of *E. coli* cells BL21 C41 (DE3) or pRARE
398 (DE3) containing plasmids harboring the constructs of the macrodomain proteins was inoculated
399 into 10 mL LB media and grown overnight at 37°C with shaking at 250 rpm. For most proteins,
400 the overnight culture was transferred to a shaker flask containing TB media at 37°C until the
401 OD600 reached 0.7. The proteins were either induced with either 0.4 mM (SARS-CoV-2 proteins)
402 or 0.05 mM (MERS-CoV proteins) IPTG at 17°C for 20 hours. Cells were pelleted at 3500 × g for
403 10 min and frozen at -80°C. Frozen cells were thawed at room temperature, resuspended in 50 mM
404 Tris (pH 7.6), 150 mM NaCl, and sonicated using the following cycle parameters: Amplitude:
405 50%, Pulse length: 30 seconds, Number of pulses: 12, while incubating on ice for >1min between
406 pulses. The soluble fraction was obtained by centrifuging the cell lysate at 45,450 × g for 30
407 minutes at 4°C. The expressed soluble proteins were purified by affinity chromatography using a
408 5 ml prepacked HisTrap HP column on an AKTA Pure protein purification system (GE

409 Healthcare). The fractions were further purified by size-exclusion chromatography (SEC) with a
410 Superdex 75 10/300 GL column equilibrated with 20mM Tris (pH 8.0), 150 mM NaCl and the
411 protein sized as a monomer relative to the column calibration standards. For the SARS-CoV-2
412 N1062A protein several modifications to this protocol were made to obtain stable soluble protein.
413 First, the overnight culture was transferred to LB instead of TB and grown to OD600 0.5 before
414 the protein was induced with 0.05 mM IPTG at 17°C for 20 hours. Cells were resuspended in water
415 prior to sonication. Tris and NaCl were added after sonication. The cell lysate was then incubated
416 with HIS-select HF Nickel Affinity Gel (Millipore-Sigma) overnight, rotating at 4°C. The lysate
417 was then passed into gravity flow chromatography. Columns were washed with 0.5M NaCl and
418 50 mM Tris-Cl pH 8 and eluted with 0.5 ml of elution buffer with 0.1 M of Imidazole. Following
419 elution, the protein was immediately purified by size-exclusion chromatography as described
420 above.

421 **Isothermal Titration Calorimetry.** All ITC titrations were performed on a MicroCal PEAQ-ITC
422 instrument (Malvern Pananalytical Inc., MA). All reactions were performed in 20 mM Tris pH 7.5,
423 150 mM NaCl using 100 μM of all macrodomain proteins at 25°C. Titration of 2 mM ADP-ribose
424 or ATP (MilliporeSigma) contained in the stirring syringe included a single 0.4 μL injection,
425 followed by 18 consecutive injections of 2 μL. Data analysis of thermograms was analyzed using
426 one set of binding sites model of the MicroCal ITC software to obtain all fitting model parameters
427 for the experiments.

428 **Differential Scanning Fluorimetry (DSF)**. Thermal shift assay with DSF involved use of
429 LightCycler® 480 Instrument (Roche Diagnostics). In total, a 15 μL mixture containing 8X
430 SYPRO Orange (Invitrogen), and 10 μM macrodomain protein in buffer containing 20 mM Hepes,
431 NaOH, pH 7.5 and various concentrations of ADP-ribose were mixed on ice in 384-well PCR plate

432 (Roche). Fluorescent signals were measured from 25 to 95 °C in 0.2 °C/30-s steps (excitation, 470-
433 505 nm; detection, 540-700 nm). Data evaluation and Tm determination involved use of the Roche
434 LightCycler® 480 Protein Melting Analysis software, and data fitting calculations involved the
435 use of single site binding curve analysis on Graphpad Prism.

436 **AlphaScreen (AS) Assay.** The AlphaScreen reactions were carried out in 384-well plates
437 (Alphaplate, PerkinElmer, Waltham, MA) in a total volume of 40 µL in buffer containing 25 mM
438 HEPES (pH 7.4), 100 mM NaCl, 0.5 mM TCEP, 0.1% BSA, and 0.05% CHAPS. All reagents
439 were prepared as 4X stocks and 10 µL volume of each reagent was added to a final volume of 40
440 µL. All compounds were transferred acoustically using ECHO 555 (Beckman Inc) and
441 preincubated after mixing with purified His-tagged macrodomain protein (250 nM) for 30 min at
442 RT, followed by addition of a 10 amino acid biotinylated and ADP-ribosylated peptide
443 [ARTK(Bio)QTARK(Aoa-RADP)S] (Cambridge peptides) (625 nM). After 1h incubation at RT,
444 streptavidin-coated donor beads (7.5 µg/mL) and nickel chelate acceptor beads (7.5 µg/mL);
445 (PerkinElmer AlphaScreen Histidine Detection Kit) were added under low light conditions, and
446 plates were shaken at 400 rpm for 60 min at RT protected from light. Plates were kept covered and
447 protected from light at all steps and read on BioTek plate reader using an AlphaScreen 680
448 excitation/570 emission filter set. For data analysis, the percent inhibition was normalized to
449 positive (DMSO + labeled peptide) and negative (DMSO + macrodomain + peptide, no ADPr)
450 controls. The IC_{50} values were calculated via four-parametric non-linear regression analysis
451 constraining bottom (=0), top (=100), & Hillslope (=1) for all curves.

452 **MAR Hydrolase Assays**. First, a 10 µM solution of purified PAPR10-CD protein was incubated
453 for 20 minutes at 37ºC with 1 mM final concentration of β-Nicotinamide Adenine Dinucleotide (β
454 NAD^+) (Millipore-Sigma) in a reaction buffer (50 mM HEPES, 150 mM NaCl, 0.2 mM DTT, and

455 0.02% NP-40). MARylated PARP10 was aliquoted and stored at -80ºC. Next, a 0.5 (I-A/F-A) or 5
456 (N/A) μM solution of MARylated PARP10-CD and 0.1 (I-A/F-A) or 1 (N-A) μM purified Mac1
457 protein was added in the reaction buffer (50 mM HEPES, 150 mM NaCl, 0.2 mM DTT, and 0.02%
458 NP-40) and incubated at 37 ºC for indicated times. The reaction was stopped with addition of 2X
459 Laemmli sample buffer containing 10% β-mercaptoethanol. Protein samples were heated at 95ºC
460 for 5 minutes before loading and separated onto SDS-PAGE cassette (Thermo Fisher Scientific
461 Bolt™ 4-12% Bis-Tris Plus Gels) in MES running buffer. For direct protein detection, the SDS-
462 PAGE gel was stained using InstantBlue® Protein Stain (Expedeon). For immunoblotting, the
463 separated proteins were transferred onto polyvinylidene difluoride (PVDF) membrane using
464 iBlot™ 2 Dry Blotting System (ThermoFisher Scientific). The blot was blocked with 5% skim
465 milk in PBS containing 0.05% Tween-20 and probed with anti-mono ADP-ribose binding reagent
466 MABE1076 (α-MAR) (Millipore-Sigma) and anti-GST tag monoclonal antibody MA4-004
467 (ThermoFisher Scientific). The primary antibodies were detected with secondary infrared anti-
468 rabbit and anti-mouse antibodies (LI-COR Biosciences). All immunoblots were visualized using
469 Odyssey® CLx Imaging System (LI-COR Biosciences). The images were quantitated using Image
470 J (National Institutes for Health (NIH)) or Image Studio software.
471 **Molecular Dynamics (MD) Simulations.** 25 ns simulations were performed for WT and I1153A
472 protein in the presence and absence of ADP-ribose using GROMACS 2019.4 [44]. Protein
473 structures used were ADP-ribose-bound SARS-2-CoV Mac1, PDB 6W02 [45], and unbound
474 SARS-2-CoV Mac1, PDB 7KQO [46]. The simulations were prepared, including virtual
475 mutagenesis, using CHARMM-GUI's Solution Builder [47], which was used to build a solvated,
476 rectangular box around one protein, parameterize the ligand, add ions to neutralize the system, set
477 up periodic boundary conditions, and generate the files to perform a gradient based minimization,

478 100 ps equilibration with a NVT ensemble, and then a 25 ns production run with an NPT ensemble
479 at 303.15 K.

480 **Cell Culture and Reagents.** Vero E6, Huh-7, Vero81, DBT, L929, HeLa cells expressing the
481 MHV receptor carcinoembryonic antigen-related cell adhesion molecule 1 (CEACAM1) (HeLa-
482 MHVR), Baby Hamster Kidney cells expressing the mouse virus receptor CEACAM1 (BHK-
483 MVR) (all gifts from Stanley Perlman, University of Iowa), AJK6, and A549-ACE2 cells (both
484 gifts from Susan Weiss, University of Pennsylvania), were grown in Dulbecco's modified Eagle
485 medium (DMEM) supplemented with 10% fetal bovine serum (FBS). Calu-3 cells (ATCC) were
486 grown in MEM supplemented with 20% FBS. Bone marrow-derived macrophages (BMDMs)
487 sourced from PARP12$^{+/+}$ and PARP12$^{-/-}$ mice were differentiated into M0 macrophages by
488 incubating cells in Roswell Park Memorial Institute (RPMI) media supplemented with 10% FBS,
489 sodium pyruvate, 100 U/ml penicillin and 100 mg/ml streptomycin, L-glutamine, M-CSF
490 (Genscript) for six days. Then to differentiate into M2 macrophages, IL-4 (Peprotech Inc.) was
491 added for 1 day. Cells were washed and replaced with fresh media every other day after the 4th day.
492 Human IFN-γ was purchased from R&D Systems. Cells were transfected with either Polyjet
493 (Amgen) or Lipofectamine 3,000 (Fisher Scientific) per the instructions of the manufacturers.

494 **Generation of Recombinant pBAC- JHMV, pBAC-MERS-CoV, and pBAC-SARS-CoV-2**
495 **Constructs.** All recombinant pBAC constructs were created using Red recombination with several
496 previously described CoV BACs as previously described [37]. These include the WT-SARS-CoV-
497 2 BAC based off the Wuhan-Hu-1 isolate provided by Sonia Zuñiga, Li Wang, Isabel Sola and
498 Luis Enjuanes (CNB-CSIC, Madrid, Spain) [41], a MERS-CoV mouse-adapated BAC (a gift from
499 Dr. Stanley Perlman) with GFP inserted into ORF5 [42, 43], and an MHV BAC based off of the
500 JHMV isolate [21]. Primers used to create each mutation are listed in Table 2.

501 **Reconstitution of Recombinant pBAC-JHMV, pBAC-MERS-CoV, and pBAC-SARS-CoV-**
502 **2-Derived Virus.** All work with SARS-CoV-2 and MERS-CoV was conducted in either the
503 University of Kansas or the Oklahoma State University EHS-approved BSL-3 facilities. To
504 generate SARS- CoV-2 or MERS-CoV, approximately 5×10^5 Huh-7 cells were transfected with
505 2 μg of purified BAC DNA using Lipofectamine 3,000 (Fisher Scientific) as a transfection reagent.
506 SARS-CoV-2 generated from these transfections (p0) was then passaged in Vero E6 (SARS-CoV-
507 2) or Vero 81 (MERS-CoV) cells to generate viral stocks (p1). All p1 stocks were again sequenced
508 by Sanger sequencing to confirm that they retained the correct mutations. To generate MHV-JHM,
509 approximately 5×10^5 BHK-MVR cells were transfected with 1 μg of purified BAC DNA and 1
510 μg of N-protein expressing plasmid using PolyJetTM Transfection Reagent (SignaGen).
511 **Mice.** Pathogen-free C57BL/6NJ (B6) and K18-ACE2 C57BL/6 mice were originally purchased
512 from Jackson Laboratories and mice were bred and maintained in the animal care facilities at the
513 University of Kansas and Oklahoma State University. Animal studies were approved by the
514 Oklahoma State University and University of Kansas Institutional Animal Care and Use
515 Committees (IACUC) following guidelines set forth in the Guide for the Care and Use of
516 Laboratory Animals.
517 **Virus Infection.** Cells were infected at the indicated MOIs. All infections included a 1 hr
518 adsorption phase. Infected cells and supernatants were collected at indicated time points and titers
519 were determined. For IFN pretreatment experiments, human IFN-γ was added to Calu-3 or A549-
520 ACE2 cells 18 to 20 h prior to infection and was maintained in the culture media throughout the
521 infection. For MHV mouse infections, 5-8 week-old male and female mice were anesthetized with
522 isoflurane and inoculated intranasally with 1×10^4 PFU recombinant MHV in a total volume of
523 12μl DMEM. MHV infected mice were scored for disease based on the following scale: 0: normal,

524 0-5% weight loss with normal movement and normal behavior; 1: mild disease, 6-12% weight
525 loss, slightly slower movement, and mild neurological issues including circling, sporadic and
526 sudden jumping/hyperreaactivity; 2: moderate disease, 13-20% weight loss, slow movement with
527 notable difficulty, moderate neurological issues including occasional circling or head pressing; 3:
528 severe, >20% decrease in weight, severely reduced mobility, and severe neurological symptoms.
529 Mice were euthanized if any of the conditions for a score of 3 were met. For SARS-CoV-2 mouse
530 infections, 12 to 16-wk-old K18-ACE2 C57BL/6 female mice were lightly anesthetized using
531 isoflurane and were intranasally infected with 2.5×10^4 PFU in 50μL DMEM. To obtain tissue for
532 virus titers, mice were euthanized on different days post challenge, lungs or brains were removed
533 and homogenized in phosphate buffered saline (PBS), and titers were determined by plaque assay
534 on either Hela-MVR (MHV) or VeroE6 (SARS-CoV-2) cells.
535 **Histopathology.** The lung lobes were perfused and placed in 10% formalin. The lung lobes were
536 then processed for H&E staining. The lung lesions were blindly scored by an American College
537 of Veterinary Pathology Board-certified pathologist. The lesions were scored on a scale of 0 to
538 10% (score 1), 10 to 40% (score 2), 40 to 70% (score 3), and >70% (score 4), and cumulative
539 scores were obtained for each mouse. The lesions scored were bronchointerstitial pneumonia,
540 perivascular inflammation, edema/fibrin, and necrosis.
541 **Real-time qPCR analysis.** RNA was isolated from cells and lungs using TRIzol (Invitrogen) and
542 cDNA was prepared using MMLV-reverse transcriptase as per manufacturer's instructions
543 (Thermo Fisher Scientific). Quantitative real-time PCR (qRT-PCR) was performed on a
544 QuantStudio3 real-time PCR system using PowerUp SYBR Green Master Mix (Thermo Fisher
545 Scientific). Primers used for qPCR were previously described [19]. Cycle threshold (C_T) values
546 were normalized to the housekeeping gene hypoxanthine phosphoribosyltransferase (HPRT) by

547 the following equation: $C_T = C_{T(\text{gene of interest})} - C_{T(HPRT)}$. Results are shown as a ratio to HPRT

548 calculated as $2^{-\Delta CT}$.

549 **Statistics.** A Student's *t* test was used to analyze differences in mean values between 2 groups,

550 for multiple group comparisons, a one-way ANOVA was used. All results are expressed as

551 means ± standard errors of the means (SEM) unless stated as standard differentiation (SD). P

552 values of ≤0.05 were considered statistically significant (*, P≤0.05; **, P≤0.01; ***, P≤0.001;

553 ****, P ≤0.0001; ns, not significant).

ACKNOWLEDGEMENTS
We thank Ivan Ahel (Oxford University) for providing protein expression plasmids, Stanley Perlman and Susan Weiss for cell lines, Stanley Perlman for critical reading of the manuscript and the MERS-CoV mouse adapted BAC, and Luis Enjuanes and Sonia Zuñiga for the SARS-CoV-2 BAC. We thank our funding from the NIH, an NIH Graduate Training grant, the University of Kansas College of Liberal Arts and Sciences, and the University of Kansas Madison and Lila Self graduate programs.

Funding:
National Institutes of Health (NIH) grant R35GM138029 (ARF)
National Institutes of Health (NIH) grant P20GM113117 (ARF)
National Institutes of Health (NIH) grant K22AI134993 (ARF)
National Institutes of Health (NIH) grant P20GM103648 (RC)
NIH Graduate Training at the Biology-Chemistry Interface grant T32GM132061 (CMK)
University of Kansas College of Liberal Arts and Sciences Graduate Research Fellowship (CMK)
University of Kansas Madison and Lila Self Scholarship and Fellowship (JJP)

The funders had no role in study design, data collection and analysis, decision to publish, or preparation of the manuscript.

Author contributions:
Conceptualization: CMK, JJP, YMA, ARF
Data curation: CMK, YMA, AR, JJOC, RG, SM, RC, ARF
Formal analysis: CMK, YMA, AR, JJOC, RG, SM, RC, ARF
Funding acquisition: CMK, RC, ARF
Methodology: CMK, JJP, YMA, AR, JJOC, RG, RK, PG, DKJ, SM, RC, ARF
Investigation: CMK, JJP, YMA, AR, JJOC, RG, RS, PM, RK, DKJ, SM, RC, ARF
Project administration: RC, ARF
Resources: AR, PG, RC, ARF
Visualization: CMK, JJP, YMA, AR, JJOC, RG, RS, PM, RK, DKJ, SM, RC, ARF
Validation: CMK, AR, SM, RC, ARF
Supervision: PG, RC, ARF
Writing—original draft: CMK, ARF
Writing—review & editing: CMK, JJP, YMA, AR, JJOC, RG, RS, PM, RK, DKJ, SM, RC, ARF

589 **REFERENCES**

590 1. Perlman S. Another Decade, Another Coronavirus. N Engl J Med. 2020;382(8):760-2. Epub
591 2020/01/25. doi: 10.1056/NEJMe2001126. PubMed PMID: 31978944; PubMed Central
592 PMCID: PMCPMC7121143.
593 2. Wolff G, Limpens R, Zevenhoven-Dobbe JC, Laugks U, Zheng S, de Jong AWM, et al. A
594 molecular pore spans the double membrane of the coronavirus replication organelle. Science.
595 2020;369(6509):1395-8. Epub 20200806. doi: 10.1126/science.abd3629. PubMed PMID:
596 32763915; PubMed Central PMCID: PMCPMC7665310.
597 3. Wang Y, Grunewald M, Perlman S. Coronaviruses: An Updated Overview of Their Replication
598 and Pathogenesis. Methods Mol Biol. 2020;2203:1-29. Epub 2020/08/25. doi: 10.1007/978-1-
599 0716-0900-2_1. PubMed PMID: 32833200; PubMed Central PMCID: PMCPMC7682345.
600 4. Lei J, Kusov Y, Hilgenfeld R. Nsp3 of coronaviruses: Structures and functions of a large multi-
601 domain protein. Antiviral Res. 2018;149:58-74. Epub 2017/11/13. doi:
602 10.1016/j.antiviral.2017.11.001. PubMed PMID: 29128390; PubMed Central PMCID:
603 PMCPMC7113668.
604 5. Leung AKL, McPherson RL, Griffin DE. Macrodomain ADP-ribosylhydrolase and the
605 pathogenesis of infectious diseases. PLoS Pathog. 2018;14(3):e1006864. Epub 2018/03/23.
606 doi: 10.1371/journal.ppat.1006864. PubMed PMID: 29566066; PubMed Central PMCID:
607 PMCPMC5864081.
608 6. Alhammad YMO, Kashipathy MM, Roy A, Gagne JP, McDonald P, Gao P, et al. The SARS-
609 CoV-2 Conserved Macrodomain Is a Mono-ADP-Ribosylhydrolase. J Virol. 2021;95(3). Epub
610 2020/11/08. doi: 10.1128/JVI.01969-20. PubMed PMID: 33158944; PubMed Central PMCID:
611 PMCPMC7925111.
612 7. Rack JG, Perina D, Ahel I. Macrodomains: Structure, Function, Evolution, and Catalytic
613 Activities. Annu Rev Biochem. 2016;85:431-54. Epub 2016/02/05. doi: 10.1146/annurev-
614 biochem-060815-014935. PubMed PMID: 26844395.
615 8. Rack JGM, Zorzini V, Zhu Z, Schuller M, Ahel D, Ahel I. Viral macrodomains: a structural
616 and evolutionary assessment of the pharmacological potential. Open Biol.
617 2020;10(11):200237. Epub 2020/11/18. doi: 10.1098/rsob.200237. PubMed PMID: 33202171;
618 PubMed Central PMCID: PMCPMC7729036.
619 9. Saikatendu KS, Joseph JS, Subramanian V, Clayton T, Griffith M, Moy K, et al. Structural
620 basis of severe acute respiratory syndrome coronavirus ADP-ribose-1"-phosphate
621 dephosphorylation by a conserved domain of nsP3. Structure. 2005;13(11):1665-75. Epub
622 2005/11/08. doi: 10.1016/j.str.2005.07.022. PubMed PMID: 16271890; PubMed Central
623 PMCID: PMCPMC7126892.
624 10. Egloff MP, Malet H, Putics A, Heinonen M, Dutartre H, Frangeul A, et al. Structural and
625 functional basis for ADP-ribose and poly(ADP-ribose) binding by viral macro domains. J
626 Virol. 2006;80(17):8493-502. Epub 2006/08/17. doi: 10.1128/JVI.00713-06. PubMed PMID:
627 16912299; PubMed Central PMCID: PMCPMC1563857.
628 11. Fehr AR, Channappanavar R, Jankevicius G, Fett C, Zhao J, Athmer J, et al. The Conserved
629 Coronavirus Macrodomain Promotes Virulence and Suppresses the Innate Immune Response
630 during Severe Acute Respiratory Syndrome Coronavirus Infection. mBio. 2016;7(6). Epub
631 2016/12/15. doi: 10.1128/mBio.01721-16. PubMed PMID: 27965448; PubMed Central
632 PMCID: PMCPMC5156301.

12. Li C, Debing Y, Jankevicius G, Neyts J, Ahel I, Coutard B, et al. Viral Macro Domains Reverse Protein ADP-Ribosylation. J Virol. 2016;90(19):8478-86. Epub 2016/07/22. doi: 10.1128/JVI.00705-16. PubMed PMID: 27440879; PubMed Central PMCID: PMCPMC5021415.
13. Suskiewicz MJ, Prokhorova E, Rack JGM, Ahel I. ADP-ribosylation from molecular mechanisms to therapeutic implications. Cell. 2023;186(21):4475-95. doi: 10.1016/j.cell.2023.08.030. PubMed PMID: 37832523.
14. Luscher B, Ahel I, Altmeyer M, Ashworth A, Bai P, Chang P, et al. ADP-ribosyltransferases, an update on function and nomenclature. FEBS J. 2021. Epub 20210729. doi: 10.1111/febs.16142. PubMed PMID: 34323016.
15. Fehr AR, Jankevicius G, Ahel I, Perlman S. Viral Macrodomains: Unique Mediators of Viral Replication and Pathogenesis. Trends Microbiol. 2018;26(7):598-610. Epub 2017/12/23. doi: 10.1016/j.tim.2017.11.011. PubMed PMID: 29268982; PubMed Central PMCID: PMCPMC6003825.
16. Fehr AR, Singh SA, Kerr CM, Mukai S, Higashi H, Aikawa M. The impact of PARPs and ADP-ribosylation on inflammation and host-pathogen interactions. Genes Dev. 2020;34(5-6):341-59. Epub 2020/02/08. doi: 10.1101/gad.334425.119. PubMed PMID: 32029454; PubMed Central PMCID: PMCPMC7050484.
17. Abraham R, Hauer D, McPherson RL, Utt A, Kirby IT, Cohen MS, et al. ADP-ribosyl-binding and hydrolase activities of the alphavirus nsP3 macrodomain are critical for initiation of virus replication. Proc Natl Acad Sci U S A. 2018;115(44):E10457-E66. Epub 2018/10/17. doi: 10.1073/pnas.1812130115. PubMed PMID: 30322911; PubMed Central PMCID: PMCPMC6217424.
18. Abraham R, McPherson RL, Dasovich M, Badiee M, Leung AKL, Griffin DE. Both ADP-Ribosyl-Binding and Hydrolase Activities of the Alphavirus nsP3 Macrodomain Affect Neurovirulence in Mice. mBio. 2020;11(1). Epub 2020/02/13. doi: 10.1128/mBio.03253-19. PubMed PMID: 32047134; PubMed Central PMCID: PMCPMC7018654.
19. Alhammad YM, Parthasarathy S, Ghimire R, Kerr CM, O'Connor JJ, Pfannenstiel JJ, et al. SARS-CoV-2 Mac1 is required for IFN antagonism and efficient virus replication in cell culture and in mice. Proc Natl Acad Sci U S A. 2023;120(35):e2302083120. Epub 20230822. doi: 10.1073/pnas.2302083120. PubMed PMID: 37607224; PubMed Central PMCID: PMCPMC10468617.
20. Eriksson KK, Cervantes-Barragan L, Ludewig B, Thiel V. Mouse hepatitis virus liver pathology is dependent on ADP-ribose-1"-phosphatase, a viral function conserved in the alpha-like supergroup. J Virol. 2008;82(24):12325-34. Epub 2008/10/17. doi: 10.1128/JVI.02082-08. PubMed PMID: 18922871; PubMed Central PMCID: PMCPMC2593347.
21. Fehr AR, Athmer J, Channappanavar R, Phillips JM, Meyerholz DK, Perlman S. The nsp3 macrodomain promotes virulence in mice with coronavirus-induced encephalitis. J Virol. 2015;89(3):1523-36. Epub 2014/11/28. doi: 10.1128/JVI.02596-14. PubMed PMID: 25428866; PubMed Central PMCID: PMCPMC4300739.
22. McPherson RL, Abraham R, Sreekumar E, Ong SE, Cheng SJ, Baxter VK, et al. ADP-ribosylhydrolase activity of Chikungunya virus macrodomain is critical for virus replication and virulence. Proc Natl Acad Sci U S A. 2017;114(7):1666-71. Epub 2017/02/02. doi: 10.1073/pnas.1621485114. PubMed PMID: 28143925; PubMed Central PMCID: PMCPMC5321000.

23. Parvez MK. The hepatitis E virus ORF1 'X-domain' residues form a putative macrodomain protein/Appr-1"-pase catalytic-site, critical for viral RNA replication. Gene. 2015;566(1):47-53. Epub 2015/04/15. doi: 10.1016/j.gene.2015.04.026. PubMed PMID: 25870943; PubMed Central PMCID: PMCPMC7127128.
24. Taha TY, Suryawanshi RK, Chen IP, Correy GJ, McCavitt-Malvido M, O'Leary PC, et al. A single inactivating amino acid change in the SARS-CoV-2 NSP3 Mac1 domain attenuates viral replication in vivo. PLoS Pathog. 2023;19(8):e1011614. Epub 20230831. doi: 10.1371/journal.ppat.1011614. PubMed PMID: 37651466; PubMed Central PMCID: PMCPMC10499221.
25. Aguilar EG, Paniccia G, Adura C, Singer ZS, Ashbrook AW, Razooky BS, et al. Sindbis Macrodomain Poly-ADP-Ribose Hydrolase Activity Is Important for Viral RNA Synthesis. J Virol. 2022;96(7):e0151621. Epub 20220317. doi: 10.1128/jvi.01516-21. PubMed PMID: 35297669; PubMed Central PMCID: PMCPMC9006893.
26. Putics A, Filipowicz W, Hall J, Gorbalenya AE, Ziebuhr J. ADP-ribose-1"-monophosphatase: a conserved coronavirus enzyme that is dispensable for viral replication in tissue culture. J Virol. 2005;79(20):12721-31. Epub 2005/09/29. doi: 10.1128/JVI.79.20.12721-12731.2005. PubMed PMID: 16188975; PubMed Central PMCID: PMCPMC1235854.
27. Grunewald ME, Chen Y, Kuny C, Maejima T, Lease R, Ferraris D, et al. The coronavirus macrodomain is required to prevent PARP-mediated inhibition of virus replication and enhancement of IFN expression. PLoS Pathog. 2019;15(5):e1007756. Epub 2019/05/17. doi: 10.1371/journal.ppat.1007756. PubMed PMID: 31095648; PubMed Central PMCID: PMCPMC6521996.
28. Kerr CM, Parthasarathy S, Schwarting N, O'Connor JJ, Pfannenstiel JJ, Giri E, et al. PARP12 is required to repress the replication of a Mac1 mutant coronavirus in a cell- and tissue-specific manner. J Virol. 2023;97(9):e0088523. Epub 20230911. doi: 10.1128/jvi.00885-23. PubMed PMID: 37695054; PubMed Central PMCID: PMCPMC10537751.
29. Russo LC, Tomasin R, Matos IA, Manucci AC, Sowa ST, Dale K, et al. The SARS-CoV-2 Nsp3 macrodomain reverses PARP9/DTX3L-dependent ADP-ribosylation induced by interferon signaling. J Biol Chem. 2021;297(3):101041. Epub 2021/08/07. doi: 10.1016/j.jbc.2021.101041. PubMed PMID: 34358560; PubMed Central PMCID: PMCPMC8332738.
30. Voth LS, O'Connor JJ, Kerr CM, Doerger E, Schwarting N, Sperstad P, et al. Unique Mutations in the Murine Hepatitis Virus Macrodomain Differentially Attenuate Virus Replication, Indicating Multiple Roles for the Macrodomain in Coronavirus Replication. J Virol. 2021;95(15):e0076621. Epub 2021/05/21. doi: 10.1128/JVI.00766-21. PubMed PMID: 34011547; PubMed Central PMCID: PMCPMC8274620.
31. Hammond RG, Schormann N, McPherson RL, Leung AKL, Deivanayagam CCS, Johnson MA. ADP-ribose and analogues bound to the deMARylating macrodomain from the bat coronavirus HKU4. Proc Natl Acad Sci U S A. 2021;118(2). doi: 10.1073/pnas.2004500118. PubMed PMID: 33397718; PubMed Central PMCID: PMCPMC7812796.
32. Karras GI, Kustatscher G, Buhecha HR, Allen MD, Pugieux C, Sait F, et al. The macro domain is an ADP-ribose binding module. EMBO J. 2005;24(11):1911-20. Epub 2005/05/20. doi: 10.1038/sj.emboj.7600664. PubMed PMID: 15902274; PubMed Central PMCID: PMCPMC1142602.
33. Neuvonen M, Ahola T. Differential activities of cellular and viral macro domain proteins in binding of ADP-ribose metabolites. J Mol Biol. 2009;385(1):212-25. Epub 2008/11/06. doi:

10.1016/j.jmb.2008.10.045. PubMed PMID: 18983849; PubMed Central PMCID: PMCPMC7094737.

34. Roy A, Alhammad YM, McDonald P, Johnson DK, Zhuo J, Wazir S, et al. Discovery of compounds that inhibit SARS-CoV-2 Mac1-ADP-ribose binding by high-throughput screening. Antiviral Res. 2022;203:105344. Epub 20220519. doi: 10.1016/j.antiviral.2022.105344. PubMed PMID: 35598780; PubMed Central PMCID: PMCPMC9119168.
35. Schuller M, Riedel K, Gibbs-Seymour I, Uth K, Sieg C, Gehring AP, et al. Discovery of a Selective Allosteric Inhibitor Targeting Macrodomain 2 of Polyadenosine-Diphosphate-Ribose Polymerase 14. ACS Chem Biol. 2017;12(11):2866-74. Epub 2017/10/11. doi: 10.1021/acschembio.7b00445. PubMed PMID: 28991428; PubMed Central PMCID: PMCPMC6089342.
36. Ekblad T, Verheugd P, Lindgren AE, Nyman T, Elofsson M, Schuler H. Identification of Poly(ADP-Ribose) Polymerase Macrodomain Inhibitors Using an AlphaScreen Protocol. SLAS Discov. 2018;23(4):353-62. Epub 20180109. doi: 10.1177/2472555217750870. PubMed PMID: 29316839.
37. Fehr AR. Bacterial Artificial Chromosome-Based Lambda Red Recombination with the I-SceI Homing Endonuclease for Genetic Alteration of MERS-CoV. Methods Mol Biol. 2020;2099:53-68. Epub 2019/12/29. doi: 10.1007/978-1-0716-0211-9_5. PubMed PMID: 31883087; PubMed Central PMCID: PMCPMC7121842.
38. Li K, Wohlford-Lenane CL, Channappanavar R, Park JE, Earnest JT, Bair TB, et al. Mouse-adapted MERS coronavirus causes lethal lung disease in human DPP4 knockin mice. Proc Natl Acad Sci U S A. 2017;114(15):E3119-E28. Epub 20170327. doi: 10.1073/pnas.1619109114. PubMed PMID: 28348219; PubMed Central PMCID: PMCPMC5393213.
39. Makrynitsa GI, Ntonti D, Marousis KD, Birkou M, Matsoukas MT, Asami S, et al. Conformational plasticity of the VEEV macro domain is important for binding of ADP-ribose. J Struct Biol. 2019;206(1):119-27. Epub 2019/03/03. doi: 10.1016/j.jsb.2019.02.008. PubMed PMID: 30825649; PubMed Central PMCID: PMCPMC7111667.
40. Hoch NC. Host ADP-ribosylation and the SARS-CoV-2 macrodomain. Biochem Soc Trans. 2021;49(4):1711-21. doi: 10.1042/BST20201212. PubMed PMID: 34351418; PubMed Central PMCID: PMCPMC8421052.
41. Roy Wong LY, Zheng J, Wilhelmsen K, Li K, Ortiz ME, Schnicker NJ, et al. Eicosanoid signaling as a therapeutic target in middle-aged mice with severe COVID-19. bioRxiv. 2021. Epub 2021/04/29. doi: 10.1101/2021.04.20.440676. PubMed PMID: 33907749; PubMed Central PMCID: PMCPMC8077574.
42. Almazan F, DeDiego ML, Sola I, Zuniga S, Nieto-Torres JL, Marquez-Jurado S, et al. Engineering a replication-competent, propagation-defective Middle East respiratory syndrome coronavirus as a vaccine candidate. mBio. 2013;4(5):e00650-13. Epub 2013/09/12. doi: 10.1128/mBio.00650-13. PubMed PMID: 24023385; PubMed Central PMCID: PMCPMC3774192.
43. Li K, Li Z, Wohlford-Lenane C, Meyerholz DK, Channappanavar R, An D, et al. Single-Dose, Intranasal Immunization with Recombinant Parainfluenza Virus 5 Expressing Middle East Respiratory Syndrome Coronavirus (MERS-CoV) Spike Protein Protects Mice from Fatal MERS-CoV Infection. mBio. 2020;11(2). Epub 20200407. doi: 10.1128/mBio.00554-20. PubMed PMID: 32265331; PubMed Central PMCID: PMCPMC7157776.

44. Van Der Spoel D, Lindahl E, Hess B, Groenhof G, Mark AE, Berendsen HJ. GROMACS: fast, flexible, and free. J Comput Chem. 2005;26(16):1701-18. doi: 10.1002/jcc.20291. PubMed PMID: 16211538.
45. Schuller M, Correy GJ, Gahbauer S, Fearon D, Wu T, Diaz RE, et al. Fragment binding to the Nsp3 macrodomain of SARS-CoV-2 identified through crystallographic screening and computational docking. Sci Adv. 2021;7(16). Epub 20210414. doi: 10.1126/sciadv.abf8711. PubMed PMID: 33853786; PubMed Central PMCID: PMCPMC8046379.
46. Michalska K, Kim Y, Jedrzejczak R, Maltseva NI, Stols L, Endres M, et al. Crystal structures of SARS-CoV-2 ADP-ribose phosphatase: from the apo form to ligand complexes. IUCrJ. 2020;7(Pt 5):814-24. Epub 2020/09/18. doi: 10.1107/S2052252520009653. PubMed PMID: 32939273; PubMed Central PMCID: PMCPMC7467174.
47. Jo S, Kim T, Iyer VG, Im W. CHARMM-GUI: a web-based graphical user interface for CHARMM. J Comput Chem. 2008;29(11):1859-65. doi: 10.1002/jcc.20945. PubMed PMID: 18351591.

784 **FIGURE LEGENDS**

785 **Figure 1. The GIF motif in loop 2 of Mac1 is highly conserved and is closely associated with**
786 **both phosphate groups and the terminal ribose of ADP-ribose.** (A) Sequence alignment of
787 Mac1 across viral and human macrodomains. GIF motif is boxed in Red. (B) Overlay of the SARS-
788 CoV-2 (purple) (6WOJ) and MERS-CoV (teal) (5HOL) Mac1 ADP-ribose binding domains with
789 ADP-ribose [6], highlighting the GIF motif and conserved asparagine and aspartic acid residues
790 discussed in the manuscript.

791 **Figure 2. MHV F1441A mutation is attenuated in cell lines and in primary cells.** DBTs (A),
792 L929s (B), and M2 macrophages (C) were infected with JHMV at an MOI of 0.1 PFU/cell. Cells
793 and supernatants were collected at indicated times and assayed for progeny infectious virus by
794 plaque assay. The data in each panel show one experiment representative of three independent
795 experiments with n = 3 for each experiment.

796 **Figure 3. MHV F1441A, but not I1440A, is partially attenuated in *in vivo*.** (A-C) Male and
797 female C57BL/6 mice were infected intranasally with WT, I1440A, and F1441A JHMV at 1×10^4
798 PFU. Mice were monitored for survival (A), weight loss (B), and disease score (as described in
799 Methods) (C) for 12 days post-infection (dpi). WT, n=4 mice; IA, n=8 mice; FA, n=8 mice. (D)
800 Brains were collected at 5 dpi and titers were determined by plaque assay. WT, n=6; IA, n=7; FA,
801 n=8. The data show the combined results from two independent experiments.

802 **Figure 4. MERS-CoV I238A and F1239A Mac1 mutations have opposing effects on ADP-**
803 **ribose binding and hydrolysis.** (A) Mac1 protein was incubated with free ADP-ribose and
804 binding affinity was measured by isothermal calorimetry as described in Methods. (B) An ADP-
805 ribosylated peptide was incubated with indicated macrodomains at increasing concentrations and
806 Alphacounts were measured as described in Methods. (C) ADP-ribose (ADPr) competition assays

807 were used to block the interaction between macrodomain proteins and ADP-ribosylation peptides
808 in the AS assay. Data was analyzed as described in Methods. The data in A-C represent combined
809 results of 2 independent experiments for each protein. (D) WT, I1153A, and F1154A MERS-CoV
810 Mac1 proteins were incubated with MARylated PARP10 CD *in vitro* at an [E]/[S] molar ratio of
811 1:5 for the indicated times at 37°C. ADP-ribosylated PARP10 CD was detected by IB with anti-
812 ADP- ribose binding reagent (MAB1076; MilliporeSigma) while total PARP10 CD protein levels
813 was detected by IB with GST antibody. The reaction with PARP10 CD incubated alone at 37°C
814 was stopped at 0 or 30 min. The image in D is representative of 2 independent experiments. (E)
815 The level of de-MARylation was measured after 30 minutes by quantifying relative band intensity
816 (ADP-ribose/GST-PARP10) using ImageJ software. Error bars represent standard deviations. The
817 results in E are the combined resulted of 2 independent experiments.

818 **Figure 5. MERS-CoV I1238A and F1239A have similarly decreased replication in human**
819 **and bat cell lines.** (A-C) Vero81 (A), Calu3 (B), and AJK6 cells (C) were infected at an MOI of
820 0.1 PFU/cell. Cells and supernatants were collected at indicated times post-infection (hpi) and
821 progeny virus was measured by plaque assay. The data in panels A, B, and C show one experiment
822 representative of three independent experiments with n = 3 for each experiment.

823 **Figure 6. SARS-CoV-2 I1153A and F1154A have increased ADP-ribose binding.** (A) SARS-
824 CoV-2 Mac1 protein was incubated with free ADP-ribose and binding affinity was measured by
825 isothermal calorimetry as described in Methods. (B) An ADP-ribosylated peptide was incubated
826 with indicated Mac1 proteins at increasing concentrations and Alphacounts were measured as
827 described in Methods. (C) WT, I1153A, and F1154A SARS-CoV-2 Mac1 proteins were incubated
828 with MARylated PARP10 CD *in vitro* at an [E]/[S] molar ratio of 1:5 for the indicated times at
829 37°C. ADP-ribosylated PARP10 CD was detected by IB with anti-ADP- ribose binding reagent

830 (MAB1076; MilliporeSigma) while total PARP10 CD protein levels were detected by IB with GST
831 antibody. The reaction with PARP10 CD incubated alone at 37°C was stopped at 0 or 30 min. The
832 data in panels A, B, and C show one experiment representative of 2 independent experiments. (D)
833 The level of de-MARylation was measured by quantifying band intensity using ImageJ software.
834 Intensity values were plotted and fitted to a nonlinear regression curve; error bars represent
835 standard deviations.

836 **Figure 7. SARS-CoV-2 N1062A binds to ADP-ribose but is highly defective in ADP-**
837 **ribosylhydrolase activity.** (A) ADP-ribosylated peptide was incubated with WT and N1062A
838 Mac1 proteins at increasing concentrations and Alphacounts were measured as described in
839 Methods. (B) ADP-ribose (ADPr) competition assays were used to block the interaction between
840 WT and N1062A Mac1 proteins and ADP-ribosylated peptides. Data was analyzed as described in
841 Methods. The data represent the means ± SD of 2 independent experiments for each protein. (C)
842 WT and N1062A Mac1 proteins (10 μM) were incubated with increasing concentrations of ADP-
843 ribose and measured by DSF as described in Methods. (D) WT and N1062A SARS-CoV-2 Mac1
844 proteins were incubated with MARylated PARP10 CD *in vitro* at an [E]/[S] molar ratio of 1:5 for
845 the indicated times at 37°C. ADP-ribosylated PARP10 CD was detected by IB with anti-ADP-
846 ribose binding reagent (green) while total PARP10 CD protein levels were detected by IB with
847 GST antibody (red). The reaction with PARP10 CD incubated alone at 37°C was stopped at 0 or
848 30 min. The data is representative of 2 independent experiments. (E) The level of de-MARylation
849 in D was measured by quantifying relative band intensity (ADP-ribose/GST-PARP10) using
850 ImageJ software. Intensity values were plotted and fitted to a nonlinear regression curve. The data
851 represent the means ± SD of 2 independent experiments for each protein.

852 **Figure 8. Increased binding has detrimental effects on SARS-CoV-2 replication in the**
853 **presence of IFNγ.** Calu3 (A) and A549-ACE2 (B) cells were pretreated with 500 units of IFNγ
854 for 18-20 hours prior to infection. Then cells were infected at an MOI of 0.1 PFU/cell. Cells and
855 supernatants were collected at indicated times post-infection (hpi) and progeny virus was measured
856 by plaque assay. The data in panels A and B show one experiment representative of three
857 independent experiments with n = 3 for each experiment.

858 **Figure 9. SARS-CoV-2 I1153A and F1154A are highly attenuated and induce elevated**
859 **innate immune responses in the lungs of infected mice.** K18-ACE2 C57BL/6 mice were
860 infected i.n. with 2.5 x 10^4 PFU of virus. (A-B) Survival (A) and weight loss (B) were monitored
861 for 14 days. n=5 for survival and n=9 for weight loss for all groups. (C) Lungs were harvested at
862 1 dpi and viral titers were determined by plaque assay. n=6 for all groups. (D) Lungs were
863 harvested at 8 dpi and viral titers were determined by plaque assay. Dotted line indicates limit of
864 detection. n=3 for WT, n=4 for I1153A and F1154A. (E) Lungs were harvested at 1 dpi in Trizol
865 and RNA was isolated. Transcripts levels were determined using qPCR with the ΔCT method.
866 n=6 for all groups. (F) Photomicrographs (hematoxylin and eosin stain) of lungs infected mice at
867 8 dpi demonstrating bronchointerstitial pneumonia (black arrow) and edema and fibrin (open
868 arrow) (G) Mice were scored for bronchointerstitial pneumonia, inflammation, and edema/fibrin
869 deposition (each on a 0-5 scale). Bar graphs represent cumulative lung pathology score in WT
870 n=3, I1153A n=4, F1154A n=4.

871 **Figure 10. Models of isoleucine-to-alanine mutation on Mac1 structure and virus replication.**
872 (A) Molecular simulation of the ADP-ribose binding domain of the SARS-CoV-2 Mac1 protein
873 was performed in absence and presence of ADP-ribose. The 1 ns averaged I/A1153 to G1069
874 distance was measured through the course of four 25 ns MD simulations of ADP-ribose bound and

875 unbound WT and I1153A protein. (B-C) A representative image at 12 ns of the simulation
876 demonstrating the distance between the I1153 and A1153 residues and G1069 at 12 ns into the
877 simulation without ADP-ribose in a space-filling (B) or stick model (C). (D) (Left) In the presence
878 of IFNγ, the WT SARS-CoV-2 Mac1 removes ADP-ribose from specific proteins (red and blue)
879 that have an ADP-ribose on an acidic reside which enhances virus replication. (Right) Due to the
880 open conformation of SARS-CoV-2 I1153A Mac1 protein, it binds to ADP-ribose bound to non-
881 acidic residues (gold and green). Since Mac1 cannot remove proteins from non-acidic residues,
882 this limits its ability to interact with relevant substrate, and the ADP-ribose remains on its normal
883 target proteins leading to poor virus replication.
884
885

886 **Table 1.** Summary of Mac1 ADP-ribose binding, hydrolysis, and replication activity

Virus	MERS-CoV				SARS-CoV-2			
Mutation	WT	N1147A	I1238A	F1239A	WT	N1062A	I1153A	F1154A
Binding	+++	nd	++++	+	+++	++	++++	++++
Hydrolysis	+++	nd	++	+	+++	+	+++	+
Replication*	+++	+	+	+	+++	++	+	+

887 nd, not determined

888 *SARS-CoV-2 replication is defined in the presence of IFNγ

889

890 **Table 2. Primers for generating recombinant CoV BACs**

Viral Strain	Forward 5'-3'	Reverse 5'-3'
MHV-CoV		
N1347A	TTTGCGCAGAGTTGGTGCTGAAGTCATCGTCAACCCTGCT GCTGGGCGCATGGCTCATGGaggatgacgacgataagtaggg	TAGCACCTGCAACACCCGCACCATGAGCCATGCGCCCAGCAGCAGGGTTGACG ATGACTTgccagtgttacaaccaattaacc
I1440A	TAAGTGTGACAATGTTGTCACCACTTTAATTTCGGCTGGTG CATTTAGTGTGCCTACTGAaggatgacgacgataagtaggg	CAAGTAGATAAGTTAAGGAAACATCAGTAGGCACACTAAATGCACCA GCCGAAATTAAAGgccagtgttacaaccaattaacc
F1441A	GTGTGACAATGTTGTCACCACTTTAATTTCGGCTGGTATAG CTAGTGTGCCTACTGATGTaggatgacgacgataagtaggg	CAAGTAGATAAGTTAAGGAAACATCAGTAGGCACACTAGCTATACCA GCCGAAATTAAAGgccagtgttacaaccaattaacc
SARS-CoV-2		
N1062A	TAAAAAGGTAAAACCAACAGTGGTTGTTAATGCAGCCGCT GTTTACCTTAAACATGGAGGaggatgacgacgataagtaggg	TTAAGGCTCCTGCAACACCTCCTCCATGTTTAAGGTAAACAGCGGCT GCATTAACAACCAgccagtgttacaaccaattaacc
I1153A	GCACGAAGTTCTACTTGCACCATTATTATCAGCTGGTGCTT TTGGTGCTGACCCTATACAaggatgacgacgataagtaggg	CTACACAAACTCTTAAAGAATGTATAGGGTCAGCACCAAAAGCACCA GCTGATAATAATGgccagtgttacaaccaattaacc
F1154A	CGAAGTTCTACTTGCACCATTATTATCAGCTGGTATTGCTG GTGCTGACCCTATACATTCaggatgacgacgataagtaggg	TATCTACACAAACTCTTAAAGAATGTATAGGGTCAGCACCAGCAATAC CAGCTGATAATAgccagtgttacaaccaattaacc
MERS-CoV.MA		
GFP	AAATTGTTCATTCTTATCCCATTTTACATCATCCAGGATTTT AACGAACTatggtgagcaagggcgagga	ACTAATGGATTAGCCTCTACACGGGACCCATAGTAGCGCAGAGCTGC TTActtgtacagctcgtccatgc
N1147A	AGCCAAGTGCTATGGGGAGTCTGTGTTAGTTAATGCTGCT GCCACACATCTTAAGCATGGaggatgacgacgataagtaggg	TAGCACCAGCGATACCACCGCCATGCTTAAGATGTGTGGCAGCAGCA TTAACTAACACAGgccagtgttacaaccaattaacc
I1238A	GCATATCCTCTTGTAGTCACTCCTCTTGTTTCAGCAGGCG CATTTGGTGTAAAACCAGCTaggatgacgacgataagtaggg	AATAAGATAATCAAAAGACACAGCTGGTTTTACACCAAATGCGCCTGC TGAAACAAGAGgccagtgttacaaccaattaacc
F1239A	ATATCCTCTTGTAGTCACTCCTCTTGTTTCAGCAGGCATAG CTGGTGTAAAACCAGCTGTaggatgacgacgataagtaggg	TCCCTAATAAGATAATCAAAAGACACAGCTGGTTTTACACCAGCTATG CCTGCTGAAACAgccagtgttacaaccaattaacc

891 Viral sequences are indicated in uppercase; marker sequences are indicated in lowercase.

A

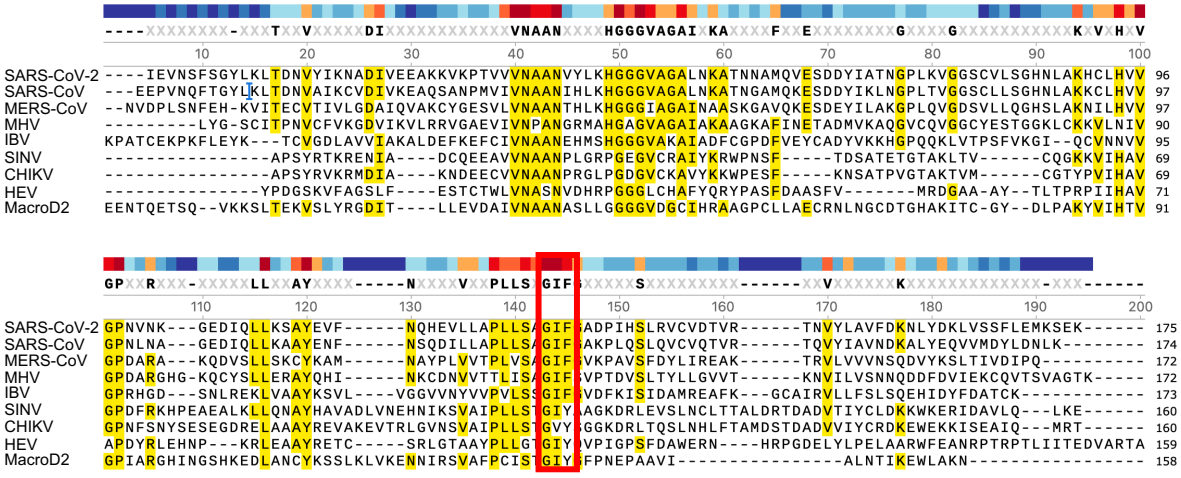

B

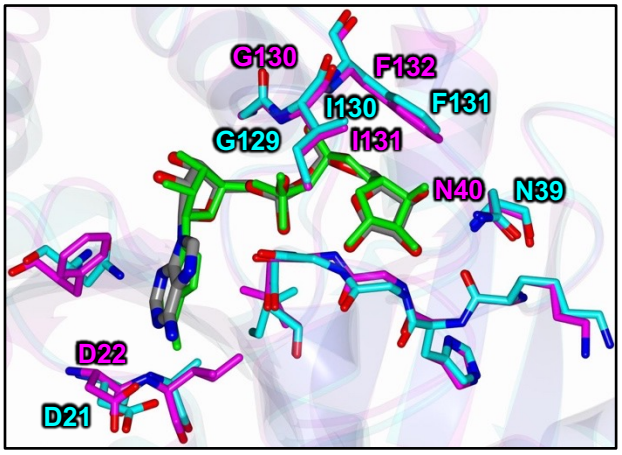

Figure 1. The GIF motif in loop 2 of Mac1 is highly conserved and is closely associated with both phosphate groups and the terminal ribose of ADP-ribose. (A) Sequence alignment of Mac1 across viral and human macrodomains. GIF motif is boxed in Red. (B) Overlay of the SARS-CoV-2 (purple) (6WOJ) and MERS-CoV (teal) (5HOL) Mac1 ADP-ribose binding domains with ADP-ribose, highlighting the GIF motif and conserved asparagine and aspartic acid residues discussed in the manuscript.

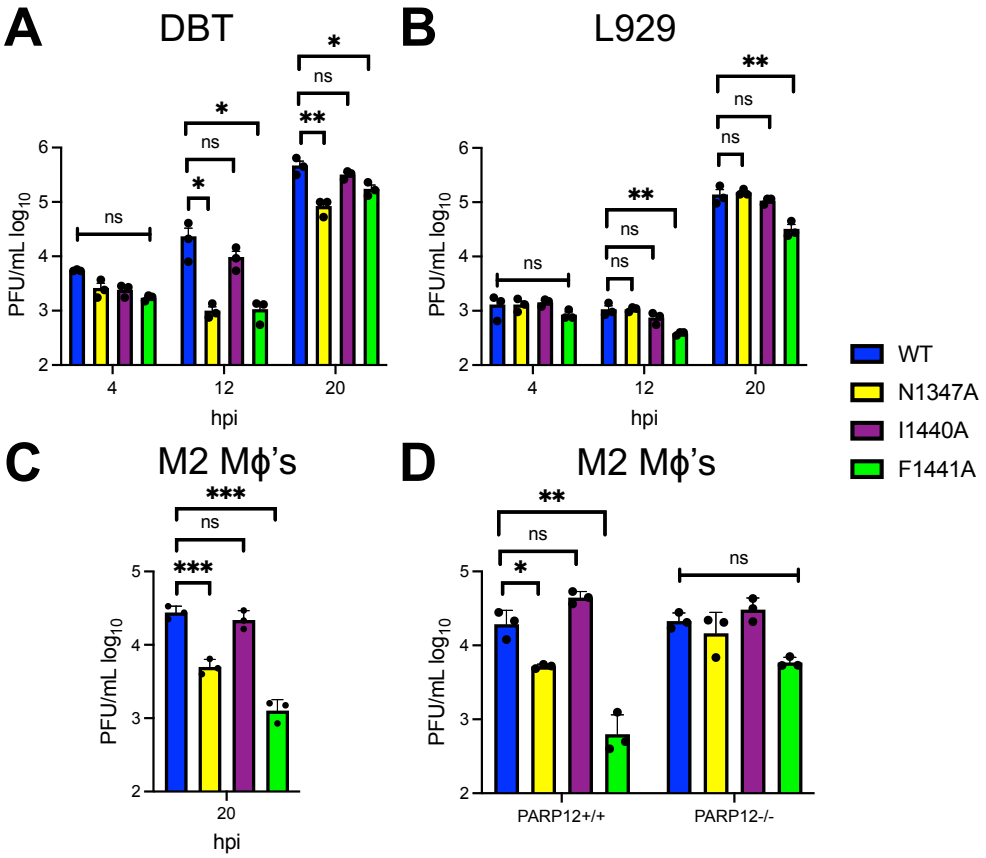

Figure 2. MHV F1441A mutation is attenuated in cell lines and in primary cells. DBTs (A), L929s (B), and M2 macrophages (C-D) were infected with JHMV at an MOI of 0.1 PFU/cell. Cells and supernatants were collected at indicated times and assayed for progeny infectious virus by plaque assay. The data in each panel show one experiment representative of three independent experiments with n = 3 for each experiment.

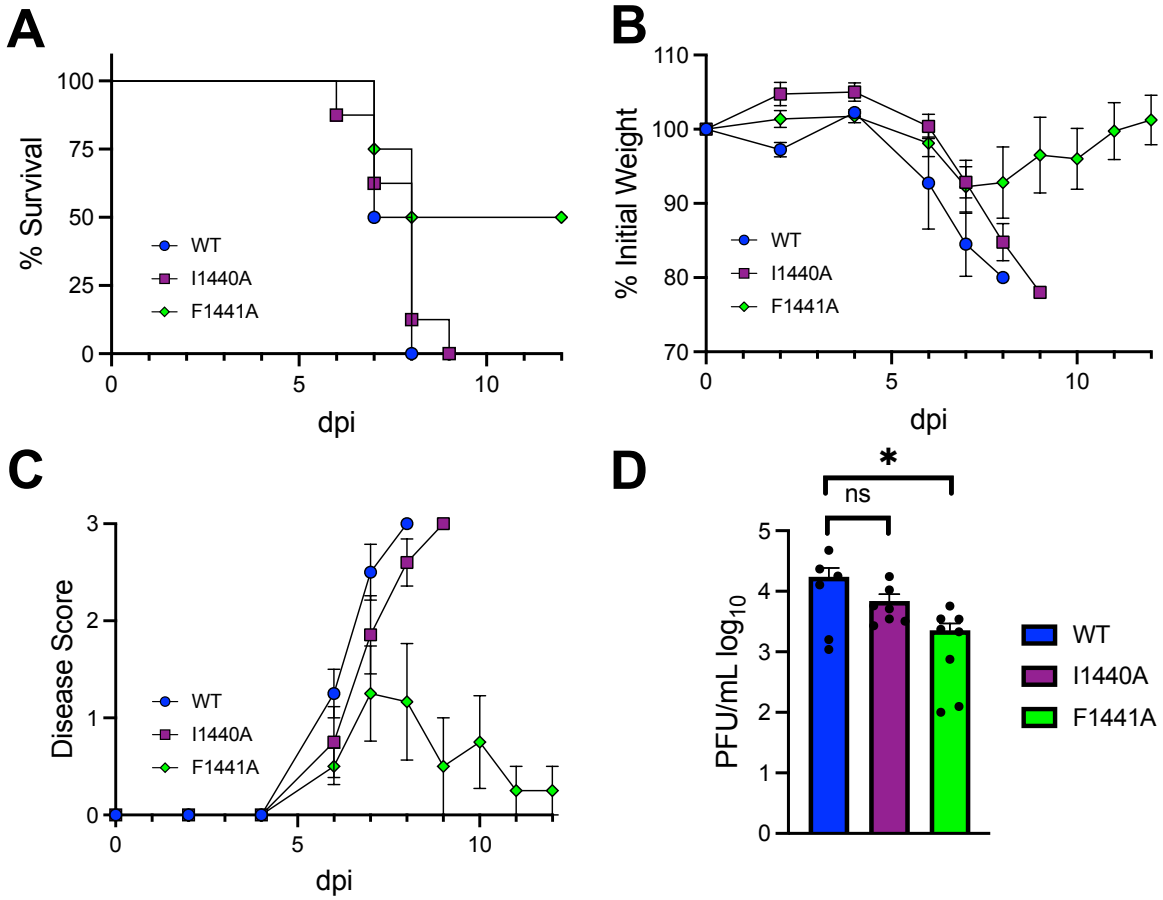

Figure 3. MHV F1441A, but not I1440A, is partially attenuated in *in vivo*. (A-C) Male and female C57BL/6 mice were infected intranasally with WT, I1440A, and F1441A JHMV at 1 X 10^4 PFU. Mice were monitored for survival (A), weight loss (B), and disease score (as described in Methods) (C) for 12 days post-infection (dpi). WT, n=4 mice; IA, n=8 mice; FA, n=8 mice. (D) Brains were collected at 5 dpi and titers were determined by plaque assay. WT, n=6; IA, n=7; FA, n=8. The data show the combined results from two independent experiments.

A

Mac1	Kd (μM)	ΔH (kcalmol^{-1})	ΔG (kcalmol^{-1})	-TΔS (kcalmol^{-1})
MERS-CoV - WT	7.2 ± 0.19	-46 ± 0.7	-29 ± 0.07	16 ± 0.6
I1238A	12.7 ± 0.21	-34 ± 1	-28 ± 0.1	6.4 ± 1
F1239A	60 ± 5	-38 ± 11	-24 ± 0.2	5 ± 1

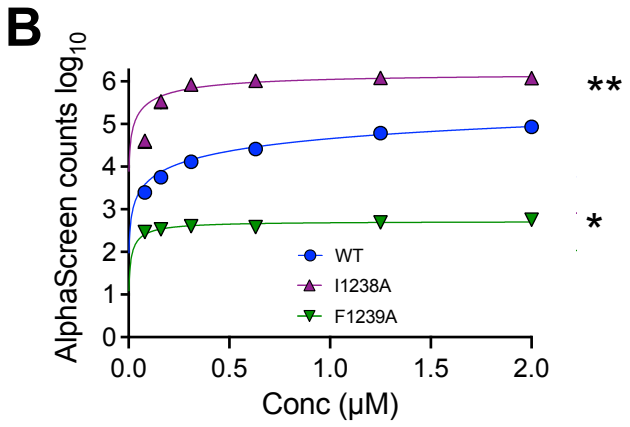

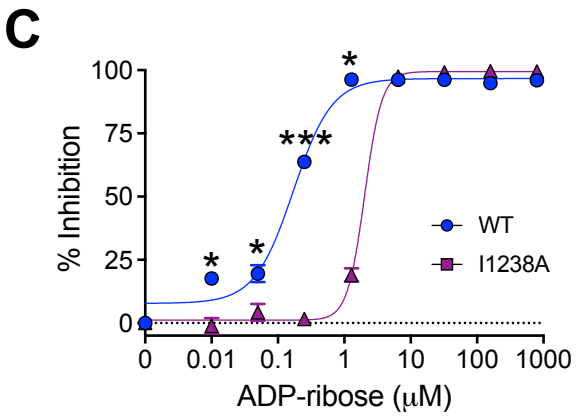

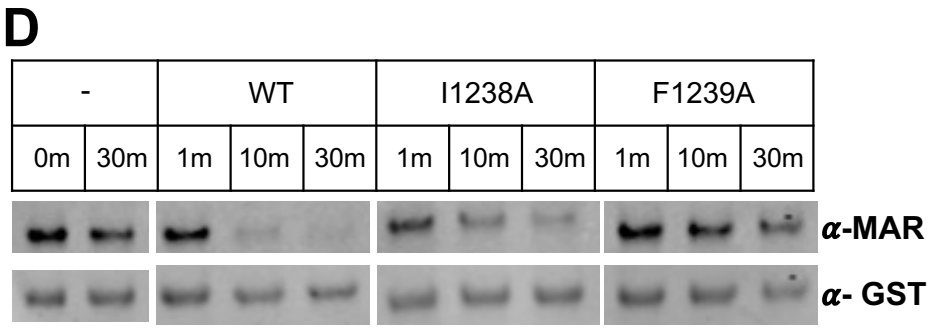

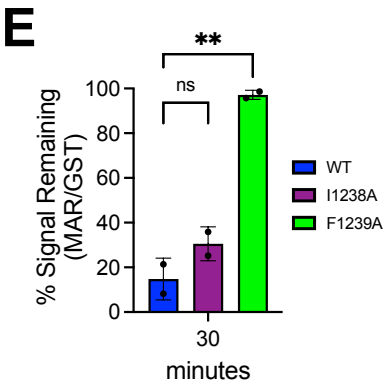

Figure 4. MERS-CoV I238A and F1239A Mac1 mutations have opposing effects on ADP-ribose binding and hydrolysis. (A) Mac1 protein was incubated with free ADP-ribose and binding affinity was measured by isothermal calorimetry as described in Methods. (B) An ADP-ribosylated peptide was incubated with indicated macrodomains at increasing concentrations and Alphacounts were measured as described in Methods. (C) ADP-ribose (ADPr) competition assays were used to block the interaction between macrodomain proteins and ADP-ribosylation peptides in the AS assay. Data was analyzed as described in Methods. The data in A-C represent combined results of 2 independent experiments for each protein. (D) WT, I1153A, and F1154A MERS-CoV Mac1 proteins were incubated with MARylated PARP10 CD in vitro at an [E]/[S] molar ratio of 1:5 for the indicated times at 37°C. ADP-ribosylated PARP10 CD was detected by IB with anti-ADP- ribose binding reagent (MAB1076; MilliporeSigma) while total PARP10 CD protein levels was detected by IB with GST antibody. The reaction with PARP10 CD incubated alone at 37°C was stopped at 0 or 30 min. The image in D is representative of 2 independent experiments. (E) The level of de-MARylation was measured after 30 minutes by quantifying relative band intensity (ADP-ribose/GST-PARP10) using ImageJ software. Error bars represent standard deviations (SD). The results in E are the combined resulted of 2 independent experiments.

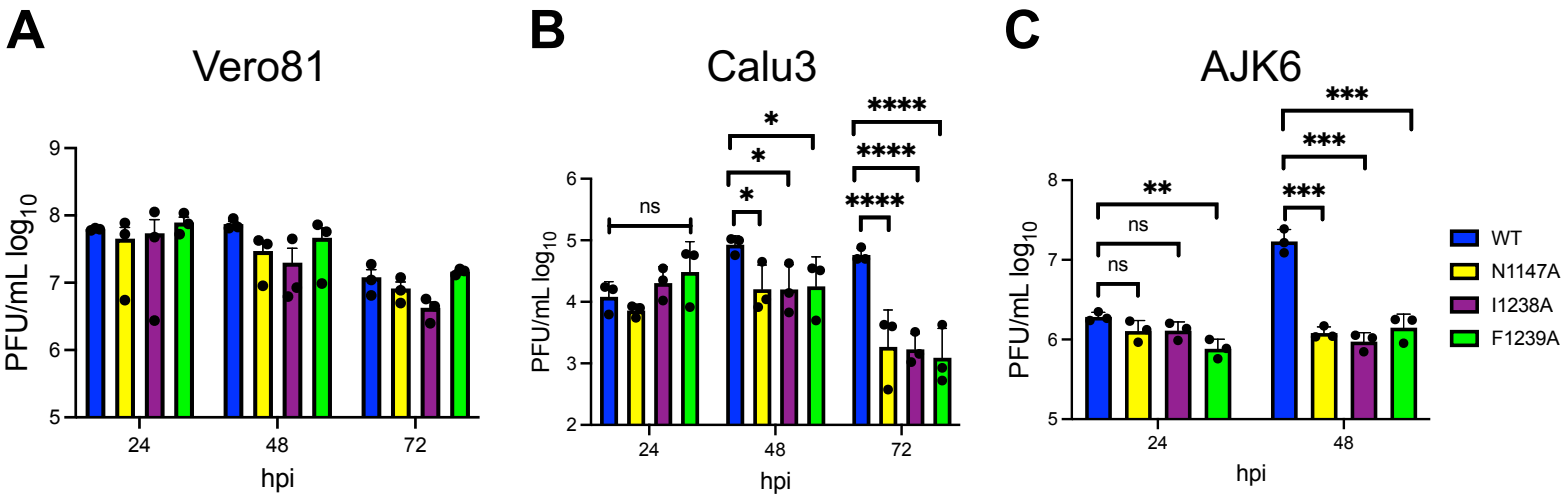

Figure 5. MERS-CoV I1238A and F1239A have similarly decreased replication in human and bat cell lines. (A-C) Vero81 (A), Calu3 (B), and AJK6 cells (C) were infected at an MOI of 0.1 PFU/cell. Cells and supernatants were collected at indicated times post-infection (hpi) and progeny virus was measured by plaque assay. The data in panels A, B, and C show one experiment representative of three independent experiments with n = 3 for each experiment.

A

Mac1	Kd (μM)	ΔH (kcalmol^{-1})	ΔG (kcalmol^{-1})	-TΔS (kcalmol^{-1})
SARS-CoV-2 - WT	16.8 ± 0.42	-28 ± 0.07	-27.3 ± 0.07	0.5 ± 0.01
I1153A	5.49 ± 0.09	-7.69 ± 0.78	-7.18 ± 0.01	0.51 ± 0.78
F1154A	5.11 ± 0.21	-6.95 ± 0.65	-7.22 ± 0.03	-0.27 ± 0.67

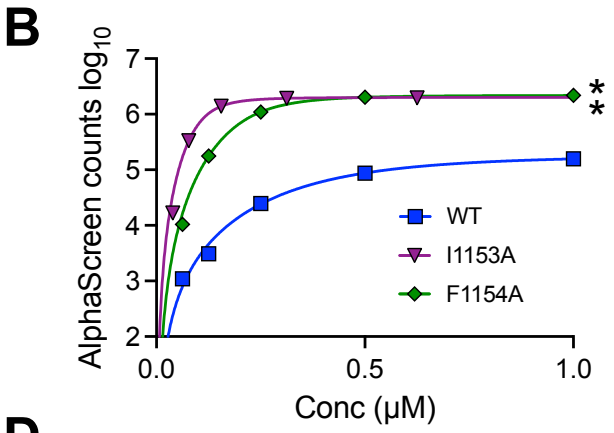

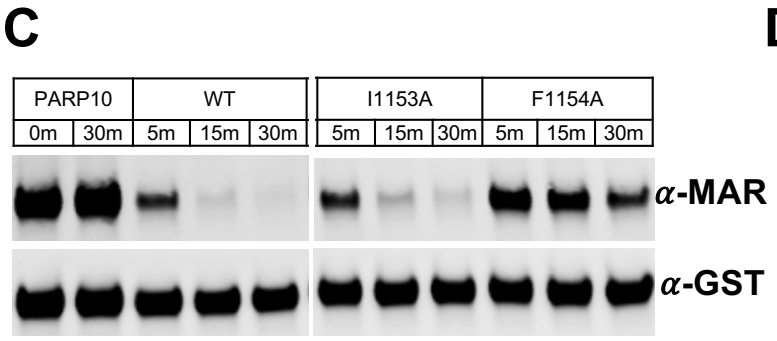

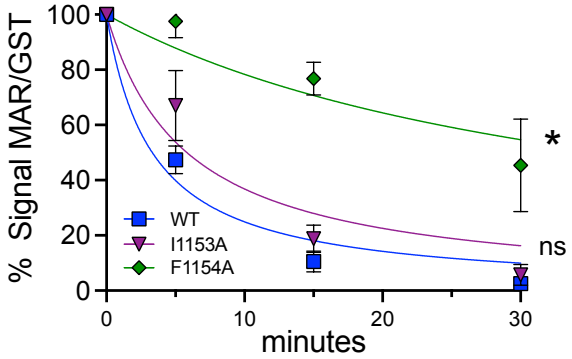

Figure 6. SARS-CoV-2 I1153A and F1154A have increased ADP-ribose binding. (A) SARS-CoV-2 Mac1 protein was incubated with free ADP-ribose and binding affinity was measured by isothermal calorimetry as described in Methods. (B) An ADP-ribosylated peptide was incubated with indicated macrodomains at increasing concentrations and Alphacounts were measured as described in Methods. (C) WT, I1153A, and F1154A SARS-CoV-2 Mac1 proteins were incubated with MARylated PARP10 CD *in vitro* at an [E]/[S] molar ratio of 1:5 for the indicated times at 37°C. ADP-ribosylated PARP10 CD was detected by IB with anti-ADP- ribose binding reagent (MAB1076; MilliporeSigma) while total PARP10 CD protein levels were detected by IB with GST antibody. The reaction with PARP10 CD incubated alone at 37°C was stopped at 0 or 30 min. The data in panels A, B, and C show one experiment representative of three independent experiments. (D) The level of de-MARylation was measured by quantifying relative band intensity (ADP-ribose/GST-PARP10) using ImageJ software. Intensity values were plotted and fitted to a nonlinear regression curve; error bars represent standard deviations.

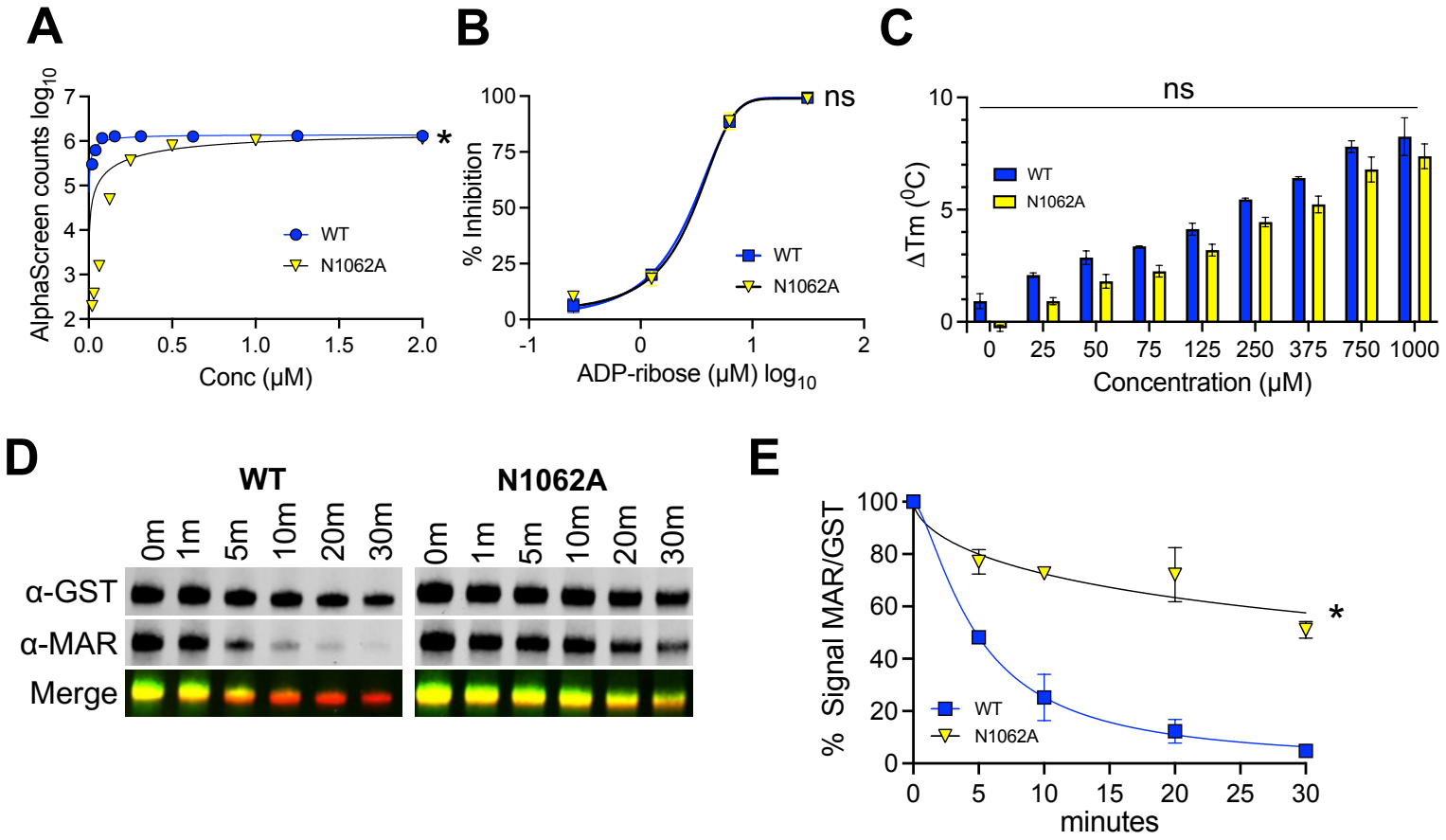

Figure 7. SARS-CoV-2 N1062A binds to ADP-ribose but is highly defective in ADP-ribosylhydrolase activity. (A) ADP-ribosylated peptide was incubated with WT and N1062A Mac1 proteins at increasing concentrations and Alphacounts were measured as described in Methods. (B) ADP-ribose (ADPr) competition assays were used to block the interaction between WT and N1062A Mac1 proteins and ADP-ribosylated peptides. Data was analyzed as described in Methods. The data represent the means ± SD of 2 independent experiments for each protein. (C) WT and N1062A Mac1 proteins (10 μM) were incubated with increasing concentrations of ADP-ribose and measured by DSF as described in Methods. (D) WT and N1062A SARS-CoV-2 Mac1 proteins were incubated with MARylated PARP10 CD *in vitro* at an [E]/[S] molar ratio of 1:5 for the indicated times at 37°C. ADP-ribosylated PARP10 CD was detected by IB with anti-ADP-ribose binding reagent (green) while total PARP10 CD protein levels were detected by IB with GST antibody (red). The reaction with PARP10 CD incubated alone at 37°C was stopped at 0 or 30 min. The data is representative of 2 independent experiments. (E) The level of de-MARylation in D was measured by quantifying relative band intensity (ADP-ribose/GST-PARP10) using ImageJ software. Intensity values were plotted and fitted to a nonlinear regression curve. The data represent the means ± SD of 2 independent experiments for each protein.

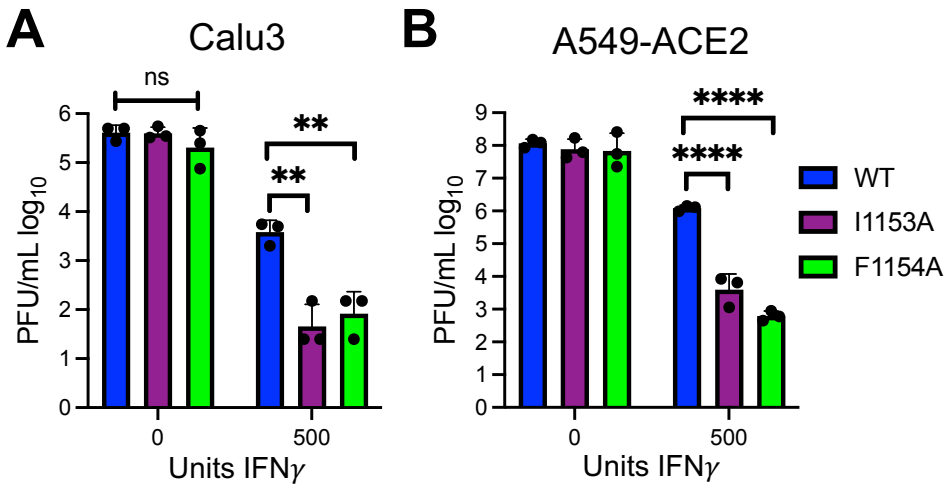

Figure 8. Increased binding has detrimental effects on SARS-CoV-2 replication in the presence of IFNγ. Calu3 (A) and A549-ACE2 (B) cells were pretreated with 500 units of IFNγ for 18-20 hours prior to infection. Then cells were infected at an MOI of 0.1 PFU/cell. Cells and supernatants were collected at 48 hpi and progeny virus was measured by plaque assay. The data in panels A and B show one experiment representative of three independent experiments with $n = 3$ for each experiment.

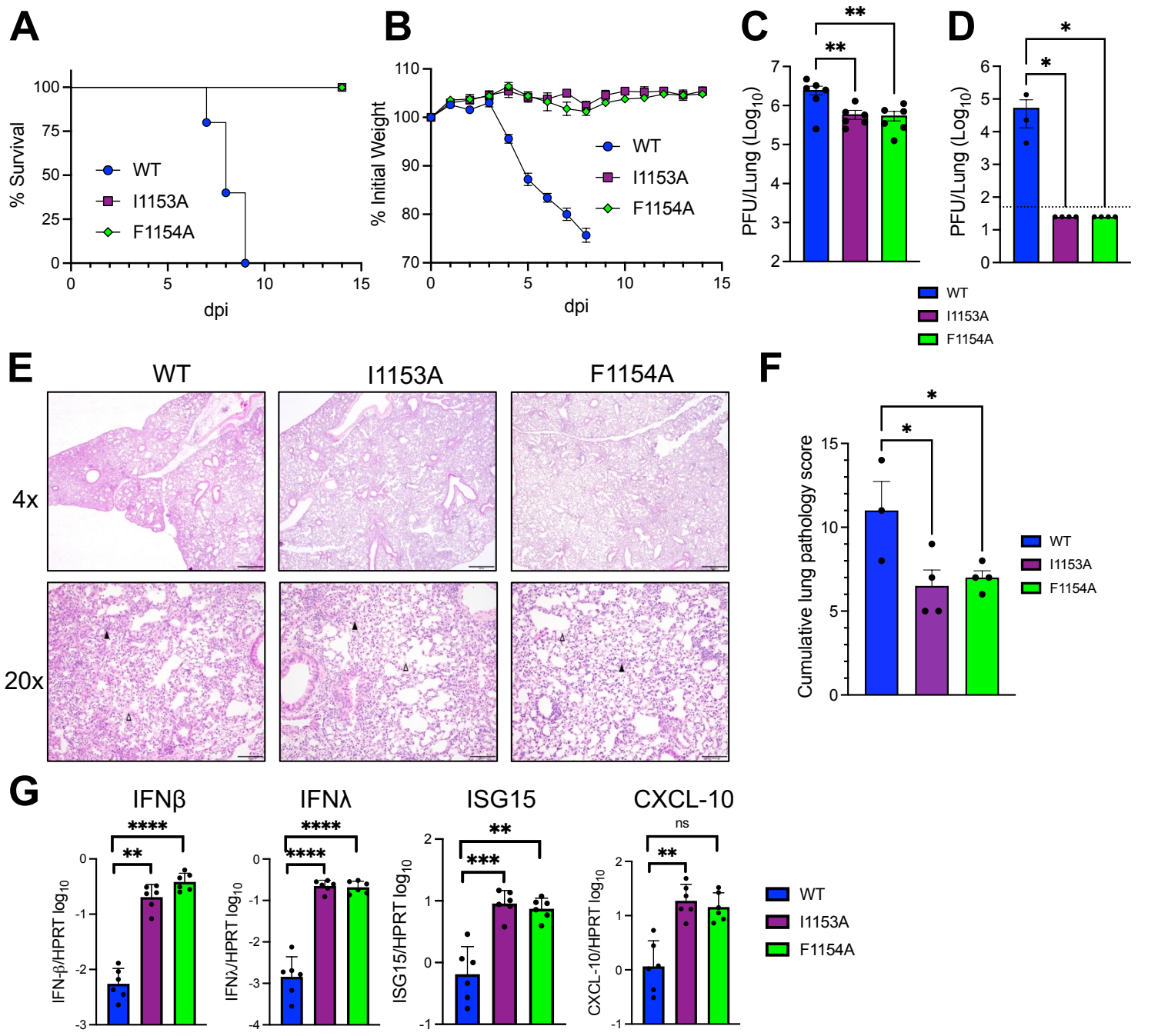

Figure 9. SARS-CoV-2 I1153A and F1154A are highly attenuated and induce elevated innate immune responses in the lungs of infected mice. K18-ACE2 C57BL/6 mice were infected i.n. with 2.5 x 10^4 PFU of virus. (A-B) Survival (A) and weight loss (B) were monitored for 14 days. n=5 for survival and n=9 for weightloss for all groups. (C) Lungs were harvested at 1 dpi and viral titers were determined by plaque assay. n=6 for all groups. (D) Lungs were harvested at 8 dpi and viral titers were determined by plaque assay. Dotted line indicates limit of detection. n=3 for WT, n=4 for I1153A and F1154A. (E) Photomicrographs (hematoxylin and eosin stain) of lungs infected mice at 8 dpi demonstrating bronchointerstitial pneumonia (black arrow) and edema and fibrin (open arrow). (F) Mice were scored for bronchointerstitial pneumonia, inflammation, and edema/fibrin deposition (each on a 0-5 scale). Bar graphs represent cumulative lung pathology score in WT n=3, I1153A n=4, F1154A n=4. (G) Lungs were harvested at 1 dpi in Trizol and RNA was isolated. Transcripts levels were determined using qPCR with the ΔCT method. n=6 for all groups.

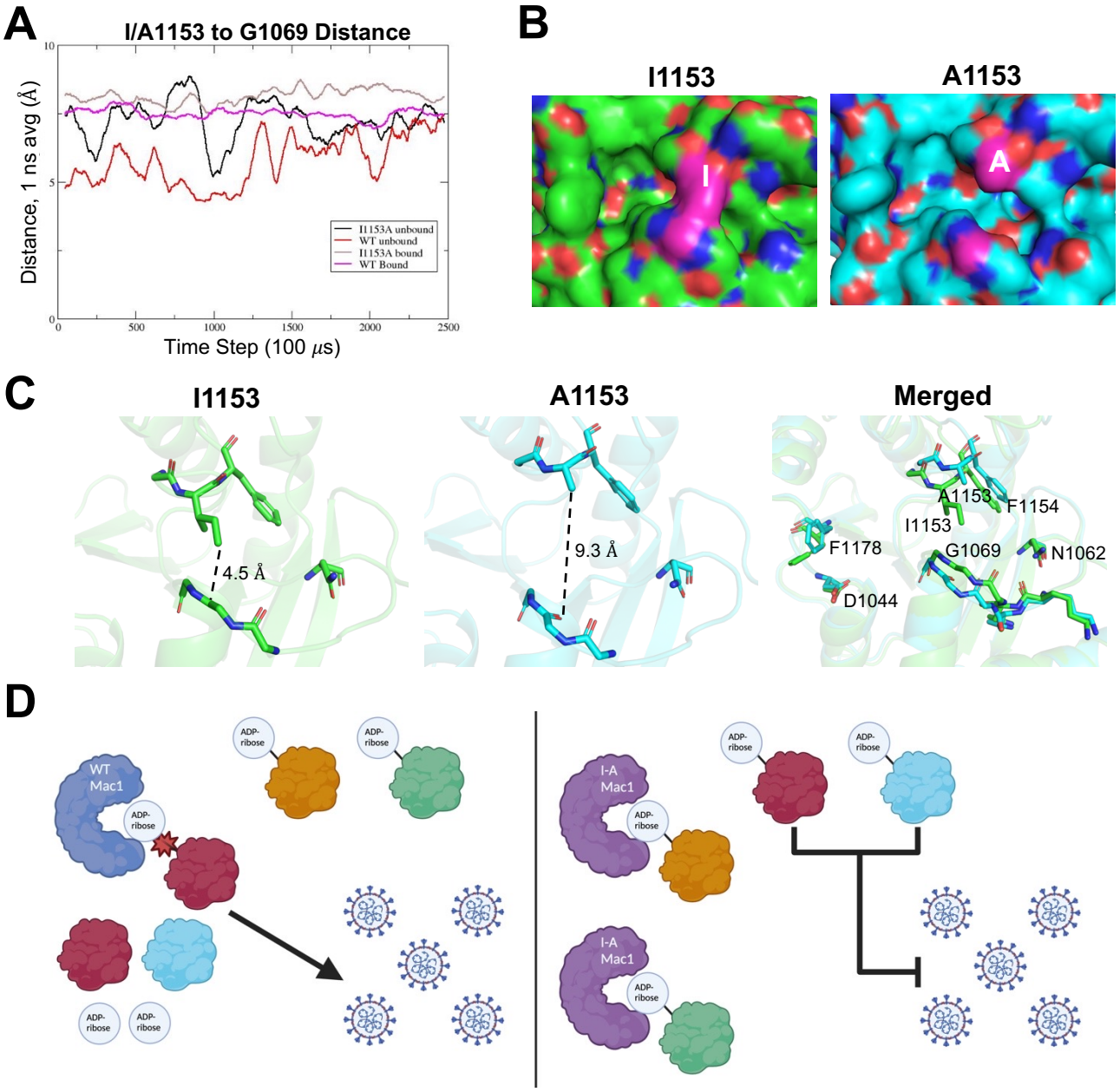

Figure 10. Models of isoleucine-to-alanine mutation on Mac1 structure and virus replication. (A) Molecular simulation of the ADP-ribose binding domain of the SARS-CoV-2 Mac1 protein was performed in absence and presence of ADP-ribose. The 1 ns averaged I/A1153 to G1069 distance was measured through the course of four 25 ns MD simulations of ADP-ribose bound and unbound WT and I1153A protein. (B-C) A representative image at 12 ns of the simulation demonstrating the distance between the I1153 and A1153 residues and G1069 at 12 ns into the simulation without ADP-ribose in a space-filling (B) or stick model (C). (D) (Left) In the presence of IFNγ, the WT SARS-CoV-2 Mac1 removes ADP-ribose from specific proteins (red and blue) that have an ADP-ribose on an acidic reside which enhances virus replication. (Right) Due to the open conformation of SARS-CoV-2 I1153A Mac1 protein, it binds to ADP-ribose bound to non-acidic residues (gold and green). Since Mac1 cannot remove proteins from non-acidic residues, this limits its ability to interact with relevant substrate, and the ADP-ribose remains on its normal target proteins leading to poor virus replication.